Seismic controls on the progress of serpentinization at ultra-slow spreading ridges

Claire Aupart[1*], Vera Schlindwein[2], Yehuda Ben-Zion[3], François Renard[1,4], and Bjørn Jamtveit[1]

[1] Physics of Geological Processes (PGP), The Njord Centre, Dept. of Geosciences, University of Oslo, PO Box 1048, N-0316, Oslo, Norway.

[2] Alfred Wegener Institute, Helmholtz Centre for Polar and Marine Research, Am Alten Hafen 26, 27568 Bremerhaven, Germany.

[3] Department of Earth Sciences, University of Southern California, Los Angeles, CA 90089, U.S.A.

[4] University Grenoble Alpes, University Savoie Mont Blanc, CNRS, IRD, IFSTTAR, ISTerre, 38000 Grenoble, France.

[*]Corresponding author: Claire Aupart (c.o.m.aupart@geo.uio.no)

Key Points:

- Earthquake-induced damage is estimated based on observed seismicity activity at several locations.
- Earthquakes produce significant rock damage along ultra-slow ridges that can enhance serpentinization.
- Extreme ridge type regimes strongly affect the extent of serpentinization at ridge axis.

Abstract

Sustained serpentinization of peridotite within the oceanic lithosphere requires effective supply of water to systems that experience continuous expansion of the solid volume. Hence, serpentinization preferentially occurs along ridge axes and in subduction zones where tectonic activity is intense and fracturing helps generating and sustaining the permeability required to connect seafloor-near environments to depth. The slowest mid-oceanic ridges produce little melt leading to discontinuous magmatic activity with very thin to no crust along most of the ridge length and up to 8 km thick crust focused around local magmatic centers. Three types of ultra-slow ridge sections can be distinguished: i) amagmatic, characterized by scarce basaltic crust and deep seismic activity, ii) magmatic, characterized by a thin basaltic crust and intermediate depth seismic activity, and iii) volcanic, characterized by a thick basaltic crust and shallow seismic activity. At amagmatic and magmatic ridge types, aseismic zones are identified above the seismic zone. The lower limit of the aseismic zone along amagmatic sections is thermally controlled and follows a 400-500˚C isotherm corresponding to the upper temperature limit for the onset of serpentinization. This observation suggests that the aseismic zone is significantly serpentinized with ample supply of water to the peridotite-serpentine interface. Based on recorded seismic activity, we estimate the associated rock volume affected by brittle damage for the different ultra-slow ridge types. We show that damage produced by seismic activity sustains pervasive serpentinization along amagmatic and magmatic types, while it is limited in the case of volcanic sections.

Plain Language Summary

Water is not limited to the Earth's surface, but also circulates deeper, where it has tremendous effects on, for example, earthquakes and volcanic activity. Seawater enters the solid Earth through fractures penetrating downwards from the seafloor. Many of these fractures form by seismic activity, particularly at seafloor ridges. Along the ridges, new seafloor forms by the rise of warm material from deeper levels, making these zones warmer than normal seafloor. Ridges show a range of temperature conditions, the colder ones being more seismically active. This study estimates how seismic activity at ridges enables water penetration and storage by using seismic data from ridge sections with different temperatures. Each earthquake is assumed to create a damaged volume that increases with the intensity of the earthquake. The total damage

created by the seismic activity is estimated as the total volume of the damage zones produced by all earthquakes occurring over a defined duration. Our results demonstrate that, at cold and intermediate temperature ridges, rocks are sufficiently damaged for water to reach down to the 400-500˚C isotherm. At warm ridges, the volume fraction of damaged rock is smaller so that water only gets access to localized zones.

1. Introduction

Serpentinization of peridotite through interaction with seawater is a widespread process with first order effects both on the chemical and physical evolution of the oceanic lithosphere (e.g. Escartin et al., 1997; Malvoisin, 2015), on the water cycle of the entire geosphere and, through associated hydrogen and methane production (Bach et al., 2006), also on the deep oceanic biosphere (e.g. Holm & Charlou, 2001; Plümper et al., 2017). Sustained water supply to the mantle is favored by a thin and permeable crust and high thermal gradients. Tectonic activity and faulting along ridge axes and subduction zones provides pathways for seawater to reach and react with mantle rocks. Hydration of young oceanic lithosphere is believed to be most efficient at slow and ultraslow oceanic ridges, where peridotite is exposed and seafloor extension is controlled by tectonics.

Until recently, serpentinization along ridge axes had only been identified within the uppermost 4-6 km depth below the seafloor along slow and ultra-slow ridges (e.g. Cannat et al., 2010; Momoh et al., 2017). Such extent has been supposed to be limited by the creation of pathways for water into fresh peridotite. In this context, serpentinization was estimated to affect ca. $2 \cdot 10^8$ m^3 of fresh peridotite per year (Cannat et al., 2010). Recent seismic studies, however, indicate that in amagmatic volumes of ultraslow ridges water supply may not be the limiting factor anymore and serpentinization may reach far deeper regions (Schlindwein & Schmid, 2016), and affect larger volumes of lithosphere. It is therefore of central importance to constrain the processes which control the extent and rate of serpentinization in such geological settings.

Serpentinization is a rapid process on ‘tectonic’ time scales with a maximum rate around 300°C for the hydration of pure forsterite (Martin & Fyfe, 1970; Malvoisin et al., 2012). Martin & Fyfe (1970) concluded that “in the serpentinization process in nature the rate of diffusion of water to the reaction site is almost certain to be rate controlling”. In systems where the rate of water supply is high, the rate of heat production by exothermic serpentinization may even be

sufficient to produce heat flow anomalies in oceanic basins (Schuiling, 1964; Delescluse & Chamot-Rooke, 2008), yet large volumes of peridotite remain unreacted even at temperatures within the stability field of serpentine. The mechanisms creating permeability clearly have first order effects on the extent of serpentinization. Numerous observations show that the positive solid volume change associated with the serpentinization reaction may drive local fracturing (e.g. O'Hanley, 1992), associated reaction produced permeability (Macdonald and Fyfe 1985; Jamtveit et al., 2008), and possibly microseismicity (Horning et al., 2018). However, in a detailed study of serpentinized peridotites, Rouméjon & Cannat (2014) showed that microfractures have a consistent orientation on the 100 m scale, and suggested that the main fluid pathways during serpentinization have been initiated by tectonic and/or thermal fracturing. Reaction-driven cracking due to volume change would follow the first influx of water to the system in addition to tectonic and thermal fracturing. However, clogging effects during swelling may operate (Hövelmann et al., 2012), and there is little doubt that the most extensive serpentinization is associated with zones of tectonic deformation such as faults and shear zones where permeability can be maintained.

Based on seismic data from ultra-slow spreading ridges, Schlindwein & Schmid (2016) showed that in regions dominated by exposed peridotite, earthquake activity was confined to a depth interval leaving an essentially aseismic zone above. They inferred the lower limit of the seismic zone to represent the onset of non-brittle deformation mechanisms in the peridotite, and the upper limit to be controlled by extensive serpentinization and associated weakening of the crust at shallower depth. Interestingly, the interface between the shallow non-seismic region and the seismic zone is parallel to the Brittle-Ductile Transition Zone (BDTZ) and thus is likely temperature controlled. The temperature of this transition zone, inferred by assuming a constant thermal gradient from the BDTZ to the seafloor, is in the range 400-500˚C. This coincides with temperatures estimated for the onset of serpentinization of abyssal peridotites (e.g. Barnes et al., 2009; Mével, 2003; Rouméjon et al., 2015). Mével (2003) suggested that the hydration boundary at slow and ultra-slow ridges may be limited by the 500˚C isotherm. Temperature control on the serpentinization reaction implies that the system does not run out of water on the time scale of the reaction. This requires connected permeability towards near ocean-floor environments, and sustained generation of reactive surface area of unaltered peridotite, despite of the large reaction-induced volume increase taking place.

Here we examine the hypothesis that regular earthquake activity in fresh mantle peridotite can produce the fracturing and permeability required for sustained fluid supply to the serpentinization front based on seismic data from two segments of the South-West Indian Ridge (SWIR). Our study includes a relocation of the earthquake dataset from the SWIR oblique supersegment previously presented by Schlindwein & Schmid (2016) and by Grevemeyer et al. (2019). We use a method recently proposed by Jamtveit et al. (2018) to determine the volume of damaged rocks from the recorded seismicity, and then discuss the consequences of these results on the serpentinization process along ridge axes.

2. Earthquake data

The study area is located along the South-West Indian Ridge (SWIR), a plate boundary between Africa and Antarctica. We focus on two segments representative of ultra-slow ridge amagmatic (SWEAP segment; Figures 1,2) and volcanic (SWRUM segment; Figures 3,4) sections. The analysis employs microseismicity catalogs first presented in Schlindwein & Schmid (2016). The seismic data have been recorded using eight Ocean Bottom Seismometers (OBS) for each segment over 8 to 11 months. We have relocated the epicenters of the SWEAP segment because another study derived different locations (Grevemeyer et al., 2019). The locations from the original publication of Schlindwein & Schmid (2016) have been retained for the SWRUM segment. All the seismic events have a local magnitude (M_l) below 3.5 with a resolution of 0.1. At both sites, only earthquakes with epicenters located less than 15 km beyond the extent of the seismic network have been selected for additional analysis to ensure reliability of the data.

2.1. SWEAP oceanic ridge segment

The oblique oceanic ridge supersegment between 9°E and 16°E has one of the slowest effective opening rates on Earth, equal to 7.8mm/yr (DeMets et al., 1990; DeMets et al., 1994; Dick et al., 2003). It is a globally amagmatic section at the western end of the SWIR subdivided in three sub-sections by two magmatic centers, the Joseph Mayes Seamount and the Narrowgate magmatic segment, located about 200 km apart (Figure 1a). The SWEAP segment is located between 11°35’E-14°15’E on this supersegment west of the Narrowgate magmatic segment.

The hypocenters locations presented in Schlindwein & Schmid (2016) and Schmid & Schlindwein (2016) show large remaining phase residuals that were not fully accounted for by a priori static correction terms. The cause of these residuals is the occurrence of unusual soft sediments under four OBS that considerably delayed the S waves. Grevemeyer et al. (2019) pointed out this effect and proposed an updated relocated catalogue. We here propose our own updated relocation. We use the linearized location algorithm *Hyposat* (Schweitzer, 2001) to determine earthquake locations in a two-step procedure. We first determine station correction terms to be applied to all stations to account for the time delay caused by the layer of soft sediments. For this step, we only use the average station residuals of the best observed earthquakes of the data set to receive robust corrections. Subsequently, we locate all earthquakes applying the station corrections. In addition, we tested our location approach against using the probabilistic, nonlinear grid-search algorithm *Nonlinloc* (Lomax et al. 2000) using both the L2-norm likelihood function (Tarantola & Valette 1982) and the equal differential time likelihood function (Font et al. 2004) in an iterative approach, assessing the results as a function of root-mean-square phase residuals and spatial location accuracy as suggested by Husen & Smith (2004). A detailed description of the relocation procedure is available in the supplementary information. The shape of the seismic zone is globally conserved while the deepest hypocenters are ca. 10-15 km shallower than what was presented in Schlindwein & Schmid (2016) and Schmid & Schlindwein (2016). The depth difference is smaller for shallower earthquakes. The shift in depth is in agreement with the catalogue of Grevemeyer et al. (2019). However, their catalogue includes some shallow events on the west side of the studied area that are not present in our relocation. This difference could impact the interpretation of the results we obtain for damaged rock volumes caused by seismicity as will be discussed later, but the calculation (see Section 3.1.) depends to a first order on the global properties of the earthquake catalogues and only slightly on the exact location of the earthquakes.

The seismic activity of the SWEAP segment is confined to a 20 km wide band parallel to the ridge axial valley (Figures 1b & 2b). Local magnitudes are mostly between 1 and 2. At depth, the seismic zone undulates. The lower limit follows the BDTZ and the upper limit is approximately 8 km above, parallel to the BDTZ (Figure 1c). As the BDTZ is thermally controlled, the upper limit of the seismic zone is likely to be so too. Based on the depth of the seismic zone (Figure 1c) and the outcome of seafloor dredging (see Figure 1c of Schlindwein & Schmid, 2016), we can

classify two types of zones: amagmatic where the seismicity is the deepest and peridotite has been dredged, and magmatic where the thermal boundaries rise and mostly basalts have been dredged. We selected one zone of each type and compare their seismicity (Figure 1b-c). Note that the north side of the seismic zone shows a gradual decrease of the seismic activity, while the limit on the south side is sharp (Figure 1b). It is especially marked in the amagmatic portion (Figure 2b). This observation was interpreted to reflect the presence of an aseismic fault zone disconnecting the two sides of the ridge (Schmid & Schlindwein, 2016).

The amagmatic portion is characterized by a high relative abundance of peridotite exposure on the seafloor implying an oceanic extension controlled by tectonics and nearly no magmatic activity. This is supported by the deep seismic activity indicative of a cooler than usual thermal regime in this portion of ridge. The seismic zone is a flat layer located between 13 and 20 km depth. Above there is an aseismic zone. The seismic activity in the amagmatic portion is less intense than in the rest of the segment, with a smaller number of earthquakes but also smaller magnitude events (Figures 1c-d & 2).

The magmatic portion is characterized by its shallower seismic zone and the occurrence of basaltic rocks on the seafloor. These are the consequences of a slightly warmer thermal regime compared to the amagmatic portion producing some magmatic activity. Most of the seismic activity is comprised in a band between 10 and 17 km depth, following the undulations of the BDTZ (Figure 1c & 2d) similarly to the amagmatic portion. However, the upper limit of the seismic zone is not perfectly parallel to the BDTZ anymore. A section across the ridge axis reveals that the seismic zone has a triangular section pointing towards the seafloor (Figure 1e). The base of the triangle is formed by the 7 km thick band containing most of the seismic activity (Figure 2d) and the activity above 10 km forms the point of the triangle. The seismic activity is more intense in the magmatic portion than in the rest of the segment with more earthquakes and larger magnitudes recorded (Figures 1c & 2). An aseismic zone is again present above the seismic zone.

By comparing the depth of the BDTZ (assumed to be 600-800˚C; Harper, 1985) and the lower limit of the aseismic zone that is thermally controlled (i.e. parallel to the BDTZ), and assuming a linear thermal gradient to the surface (consistent with low magmatic regime), we infer the temperature of the base of the aseismic zone to be around 400-500˚C. This corresponds to the temperature expected for the onset of serpentinization in the oceanic lithosphere (e.g.

Barnes et al., 2009; Mével, 2003; Rouméjon et al., 2015). Serpentinization is known to induce a weakening of the rock because of the velocity strengthening frictional behavior of serpentines (Moore et al., 2004). This could explain the aseismicity of the zone. Observed P-wave velocities (Schmid & Schlindwein, 2016) are consistent with serpentinized peridotite or basaltic material. However, due to the low magmatic activity of the entire portion, the basaltic component is likely limited.

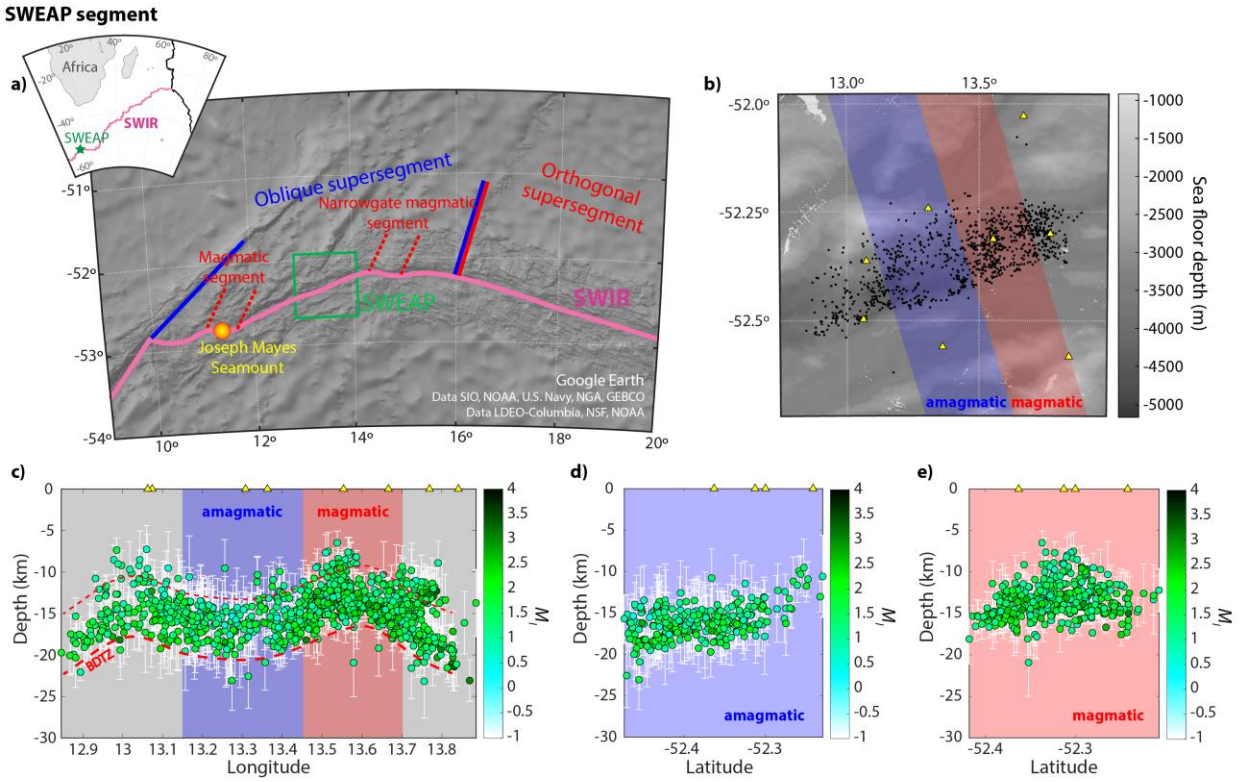

Figure 1. Location of the SWEAP segment and location of its recorded seismicity a) Location of the SWEAP segment on the SWIR and map of the oblique supersegment detailing its structure around the SWEAP segment. Blues lines define the globally amagmatic oblique supersegment. Red lines define magmatic portions and the yellow dot indicates a major volcanic seamount. Lines are dashed when included inside supersegments. The pink line represents the ridge axis. The SWEAP segment location is indicated by the green square. b) Earthquake epicenters location along the SWEAP segment. Places where no bathymetry data was available are indicated by a lighter grey color. c) Depth profile of earthquakes distribution and magnitudes along the SWEAP segment. Dashed lines indicate the BDTZ and the 400-500˚C isotherm. d) & e) Depth profile of earthquakes distribution and magnitudes across the amagmatic (d) and

magmatic (e) portions of the SWEAP segment. Blue and red zones indicate the emplacement of the amagmatic zone and the magmatic zone, respectively. In b, c, d, and e, yellow triangles show ocean bottom seismometers location.

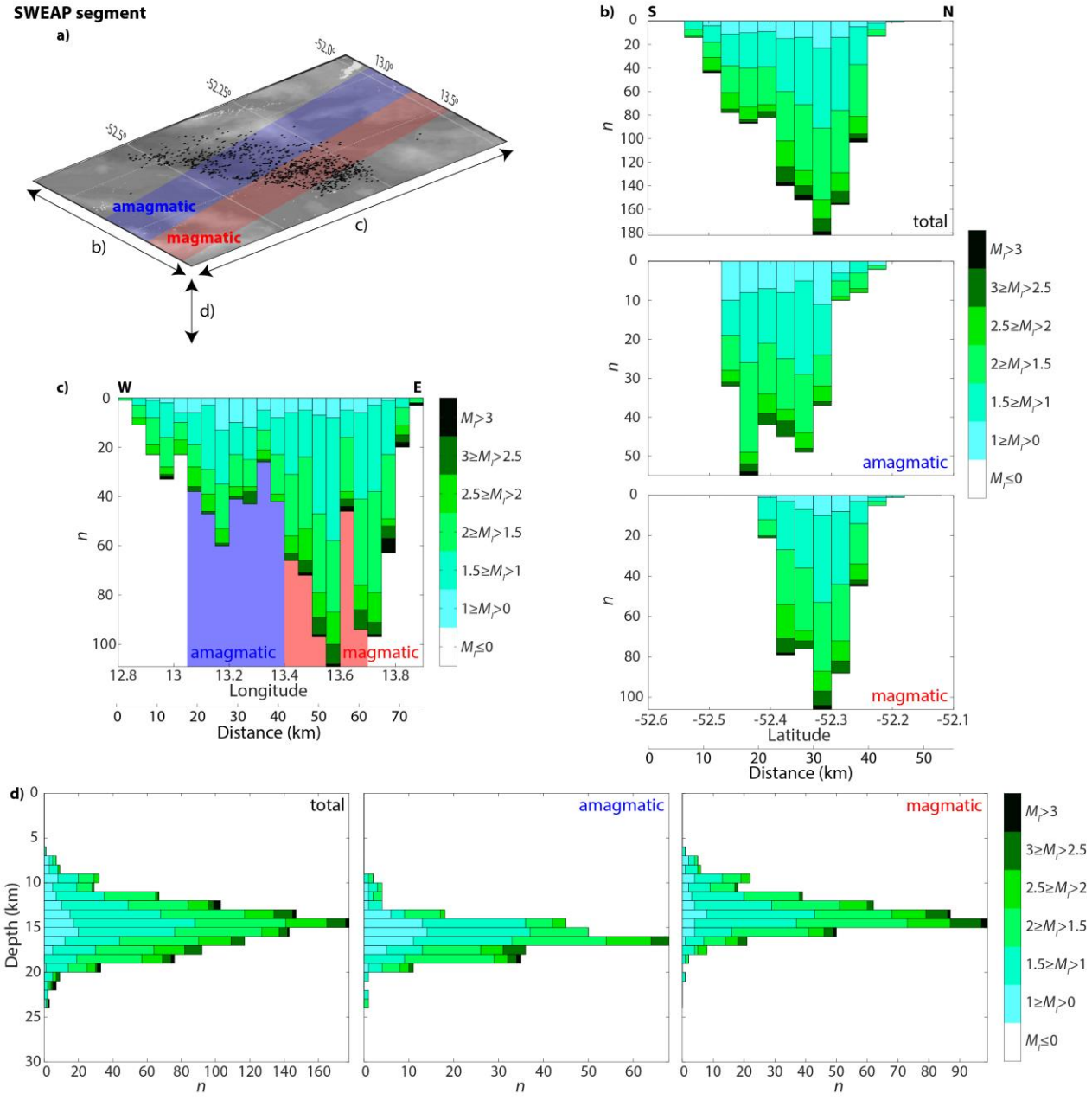

Figure 2. Spatial distribution of earthquake numbers and magnitudes for the SWEAP catalogue. a) Schematic map showing the cross-sections represented in b), c) and d). b)-d) Histograms showing the earthquakes number and magnitude spatial distributions of the SWEAP segment and

of the amagmatic and magmatic sub-segments. Spatial directions represented are latitude (b), longitude (c), and depth (d).

2.2. SWRUM oceanic ridge segment

The second study area is a volcanic section between 65°10'E and 66°05'E close to the Rodriguez Triple Junction where the African, Antarctica and Australian plates meet (SWRUM segment; Figure 3a). The opening rate at this location is 13.6 mm/yr (DeMets et al., 1990; DeMets et al., 1994). The segment is centered on a large active volcano typical of ultra-slow systems. The main volcano is assumed to feed surrounding minor magmatic centers and its eruption cycle lasts for several decades (Schmid et al., 2017). Again, the seismic activity is mostly contained in a 20 km wide band corresponding to the ridge axial valley. However, some seismic activity has been recorded outside this band and could exist outside the seismic network (Figure 3b). Under the volcano, a melt lens suppresses seismic activity (Schmid et al., 2017; Figures 3b-c & 4c). The earthquake magnitudes are in general lower than at the SWEAP segment, most of them being lower than 2 with a significant population lower than 1 (Figures 3c-d & 4). The lower limit of the seismic zone follows the BDTZ, and its thickness is slightly larger than 10 km (Figures 3c-d & 4d). The upper limit of this zone reaches the seafloor next to the volcano and dips down to a few kilometers away from it. On the western side this zone reaches ~10 km depth over a short distance, while on the eastern side it stagnates at ~5 km depth. It is correlated with enhanced seismicity (Figure 4c) due to dyke intrusion and tremor (Schmid et al., 2017; Meier & Schlindwein, 2018), and enhanced magmatic activity on the North-East side of the ridge segment. A section across the ridge axis shows an inversed V-shape of the seismic zone (Figure 3d).

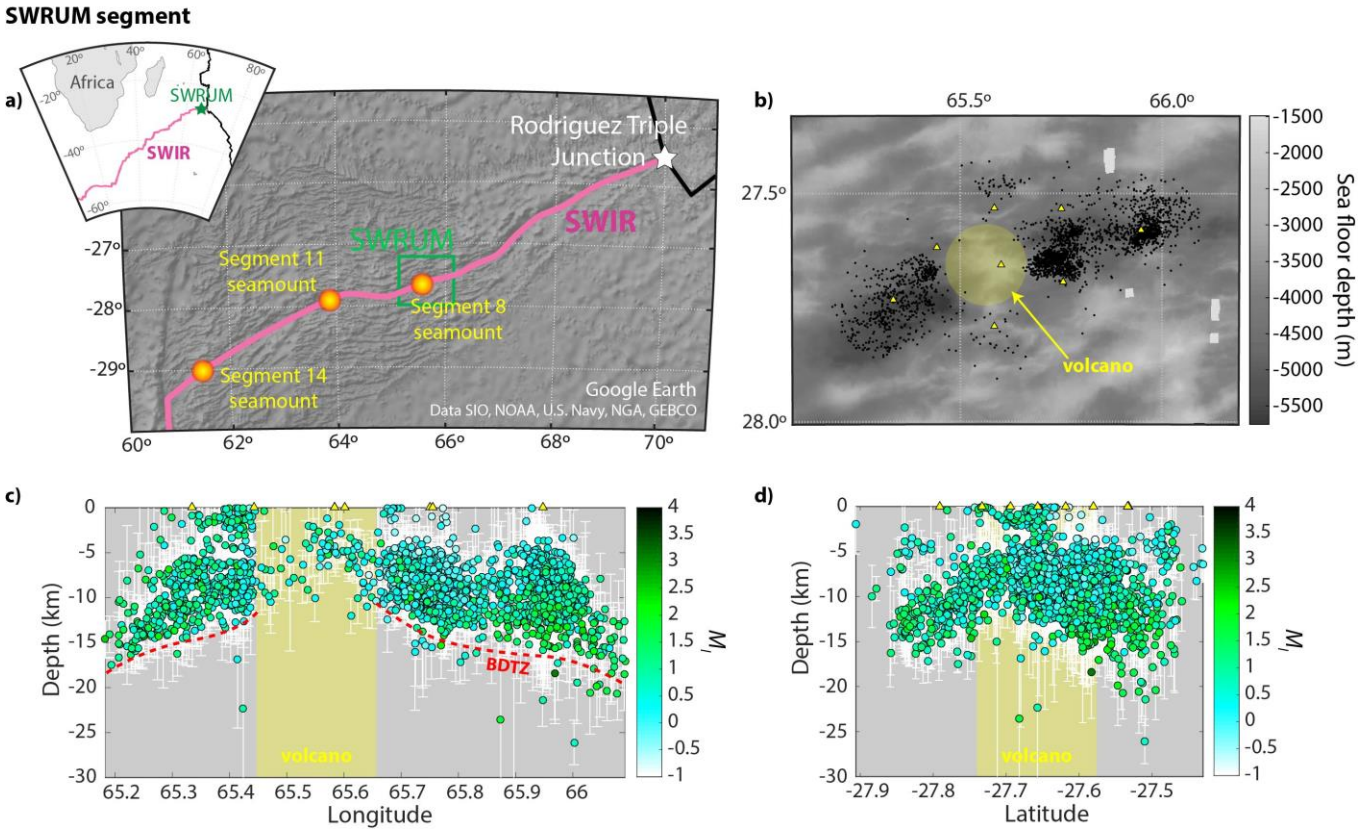

Figure 3. Location of the SWRUM segment and location of its recorded seismicity. a) Location of the SWRUM segment on the SWIR and map of the SWIR around the SWRUM segment. The yellow dots indicate major volcanic seamounts. The pink line represents the ridge axis and the black lines represent the Mid-Indian and the South-East Indian ridges. The SWRUM segment location is indicated by the green square. b) Epicenters location along the SWRUM segment. Areas where no bathymetry data was available are indicated by a lighter grey color. c) Depth profile of earthquakes distribution and magnitudes along the SWRUM segment. Dashed line indicate the BDTZ. d) Depth profile of earthquakes distribution and magnitudes across the SWRUM segment. The yellow zone indicates the region below the volcano. In b, c, and d, yellow triangles show ocean bottom seismometers location.

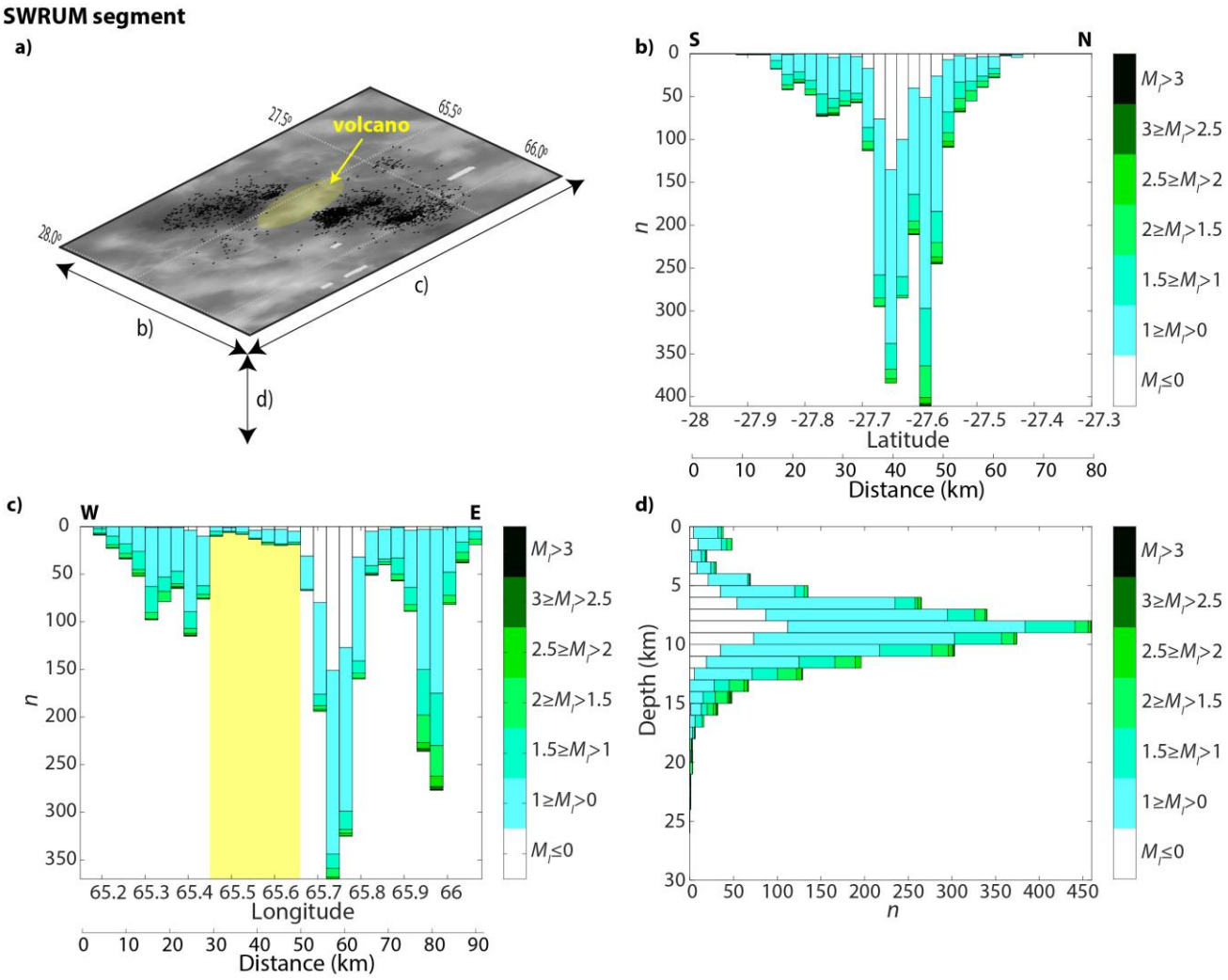

Figure 4. Spatial distribution of earthquake numbers and magnitudes for the SWRUM catalogue. a) Schematic map showing the cross-sections represented in b), c) and d). b)-d) Histograms showing the earthquakes number and magnitude spatial distributions of the SWRUM segment. Spatial directions represented are latitude (b), longitude (c), and depth (d).

3. Methods

We analyze the likelihood that seismic activity and associated fracturing may generate pervasive rock damage and associated permeability towards an eventual serpentinization front. This is done by testing if the estimated fractured (damaged) rock volume generated by the observed seismic activity is sufficient to maintain pathways for seawater to reach fresh peridotite along the different types of amagmatic, magmatic and volcanic segments. The damaged volume is calculated following the method developed by Jamtveit et al. (2018) and is based on scaling

relations from fracture mechanics and earthquake phenomenology (Ben-Zion, 2008), with estimated a- and b-values of the Gutenberg-Richter statistics in the study areas. Due to the pervasive spatial distribution of the earthquakes and their complex focal solution (Schmid & Schlindwein, 2016), we initially assume that each seismic event produces new damage volume. The likely effects of fault reactivation and damage zone overlapping are discussed in section 5.1.

3.1. Damaged volume calculation

The volume of damaged rock (V_{RD}) generated by a population of earthquakes within a magnitude range M_1 to M_2 is estimated by integrating the damage created by all earthquakes for a given study region:

$$V_{RD}(M_1 < M < M_2) = \int_{M_1}^{M_2} A(M) \cdot t_{RD}(M) \cdot n(M) \cdot dM, \quad (1)$$

where A and t_{RD} are the fracture surface area and the thickness of the damaged zone of an earthquake with magnitude M, and $n(M)$ is the density of earthquakes around magnitude M given by the Gutenberg-Richter relation. Both the fracture area and damage zone thickness increase with the earthquake magnitude.

When integrated, equation (1) leads to the following relation (Jamtveit et al., 2018):

$$V_{RD}(M_1 < M < M_2) = \beta \cdot [\exp(\alpha M_2) - \exp(\alpha M_1)] \quad (2)$$

where $\alpha = (d - b) \cdot \ln(10)$ and $\beta = \frac{\pi}{\alpha}\gamma \cdot \left(\frac{7.10^{-5}}{16\Delta\varepsilon}\right) \cdot 10^{a+e}$.

Here γ is a constant relating the damaged zone thickness to the rupture length, $\Delta\varepsilon$ is the strain drop and the formula assumes that each earthquake can be approximated by a circular rupture (Ben-Zion, 2008). For our calculations we use γ = 0.002 and $\Delta\varepsilon = 5{\cdot}10^{-5}$ as in Jamtveit et al. (2018). The constants a and b are extracted from the Gutenberg-Richter statistics of the data (see Section 3.2.), while d and e are coefficients describing the relation between seismic potency (P_0) and magnitude $\log(P_0(M)) = dM + e$. We use P_0 in km^2·cm, d = 1 and 1.34 for magnitudes smaller or larger than 3.5, respectively, and e = -4.7 and -5.22 for magnitudes smaller or larger than 3.5, respectively. These values were found to describe seismicity in a variety of regions (Ben-Zion and Zhu, 2002; Edwards et al., 2010).

3.2. Gutenberg-Richter scaling parameters

The frequency-magnitude relation $\log_{10}(n(M)) = a - bM$ (Gutenberg and Richter 1944) is a universal empirical law describing the distribution of the number of earthquakes with different magnitudes. The parameters *a* and *b* quantify the overall rate of seismicity and the relative rates of events in different magnitude ranges. The *a*-value depends on the observation time and size of the studied zone, while the *b*-value does not depend strongly on these quantities. The *a*- and *b*-values for our datasets are estimated from the cumulative distribution of earthquakes defined between the minimum and maximum magnitudes. The obtained *a*-values are normalized by the surface of study areas (length of examined ridge times the width of the seismic zone) and by the time span of the data acquisition (Table 1). This provides *a*-values and corresponding event intensity 10^a in number of earthquakes per year per km^2.

Ridge		Spreading rate (mm/yr)	Time of OBS deployment (yr)	Coordinates along the axis (latitude, longitude)	Section length (km)	Depth interval (km)
SWEAP	Total	7,8	0,94	[-52.480;12.850] [-52.265;13.890]	74,5	9
	Amagmatic section			[-52.420;13.150] [-52.350;13.450]	21,8	8
	Magmatic section			[-52.350;13.450] [-52.290;13.700]	18,2	10
SWRUM		13,6	0,65	[-27.833;65.210] [-27.700;65.450] [-27.650;65.650] [-27.500;66.080]	72,8	12

Table 1. Oceanic ridge sections characteristics used in the calculation of damage volumes. The coordinates have been determined to obtain the best possible representation of the length of the ridge affected by the selected earthquake populations and are used to calculate the section length. The SWRUM section is composed of two segments as the portion rendered aseismic by the volcano has been removed from the length estimate. The depth interval column gives the thickness of the seismic zone in depth.

A key parameter in the determination of *a*- and *b*-values is the magnitude of completeness (M_c) of the earthquake catalogues, above which all earthquakes are assumed to be recorded. The estimates of *b* and *a* are sensitive to M_c. We use three different methods to estimate M_c: the maximum curvature ($M_{c\mathrm{MAXC}}$), the goodness-of-fit ($M_{c\mathrm{GFT}}$) based on the maximization of a parameter, R_{GFT} (between 0 and 100), and the *b*-value stability ($M_{c\mathrm{MBS}}$). Details of these three methods are given in the Appendix A. The average value provided by the three methods is used as the estimate of M_c and their standard variation is used as the error on the estimated M_c.

To obtain the most accurate *a*- and *b*-values, we use linear regression. A cut-off magnitude (M_{co}) is required for large events to avoid non-significant deviation from the distribution tail of the Gutenberg-Richter scaling. We implemented two methods to estimate M_{co}. The first one identifies when the number of earthquakes recorded significantly drops (M_{codrop}). The second one is similar to the b-value stability method used to estimate M_c (M_{coMBS}). Details of these two methods are given in Appendix B. The mean value of M_{codrop} and M_{coMBS} is used as M_{co} with an error estimated as the difference between M_{codrop} and M_{coMBS} divided by 2.

Final *a*- and *b*-values are obtained by linear regression between M_c and M_{co}. The errors are estimated using the variability of M_c and M_{co}. Populations of *a*- and *b*-values are estimated for all the possible values of M_c and M_{co} within their error ranges. The error in *a* and *b* are considered to be 2 times the standard deviations of these populations.

4. Results

4.1. *a*- and *b*-values

Calculations of *a*- and *b*-values and associated damage volumes are made based on seismic data from the SWEAP and SRWUM segments. The completeness magnitude (M_c) values for the SWEAP segment and sub-segments are consistently between 1.4 and 1.6, with errors between 0.1 and 0.3 (Table 2 & Figure 5a-c). The amagmatic section has the largest uncertainty (0.3). This is due to the low number of hypocenters of this ridge portion, resulting in poor statistics. The estimate of M_c for the SWRUM segment is however much more uncertain. The MAXC method returns a value of 0.4, while the GFT and MBS methods give a value of 1.7 (Table 2 & Figure 5d). We estimate M_c for the SWRUM segment to be 1.3 with an error of 0.8. This large uncertainty is likely the consequence of the volcanic activity of the area.

Ridge		n_{tot}	$M_{c\,MAXC}$	$M_{c\,GFT}$	R_{GFT}	$M_{c\,MBS}$	$\boldsymbol{M_c}$	+/-	$M_{co\,drop}$	$M_{co\,MBS}$	$\boldsymbol{M_{co}}$	+/-	***a***	+/-	***b***	+/-
SWEAP	Total	1055	1,5	1,5	74,44	1,7	**1,6**	0,1	3,0	2,4	**2,7**	0,3	**1,11**	0,20	**0,97**	0,10
SWEAP	Amagmatic section	280	1,2	1,6	83,25	1,7	**1,5**	0,3	2,7	2,7	**2,7**	0,0	**1,05**	0,17	**1,02**	0,07
SWEAP	Magmatic section	421	1,3	1,5	75,84	1,5	**1,4**	0,1	2,5	2,5	**2,5**	0,0	**1,13**	0,07	**0,87**	0,03
SWRUM		2657	0,4	1,7	93,90	1,7	**1,3**	0,8	2,8	2,9	**2,8**	0,1	**1,25**	0,31	**1,26**	0,14

Table 2. Results of M_c, M_{co}, *a*- and *b*-values estimates.

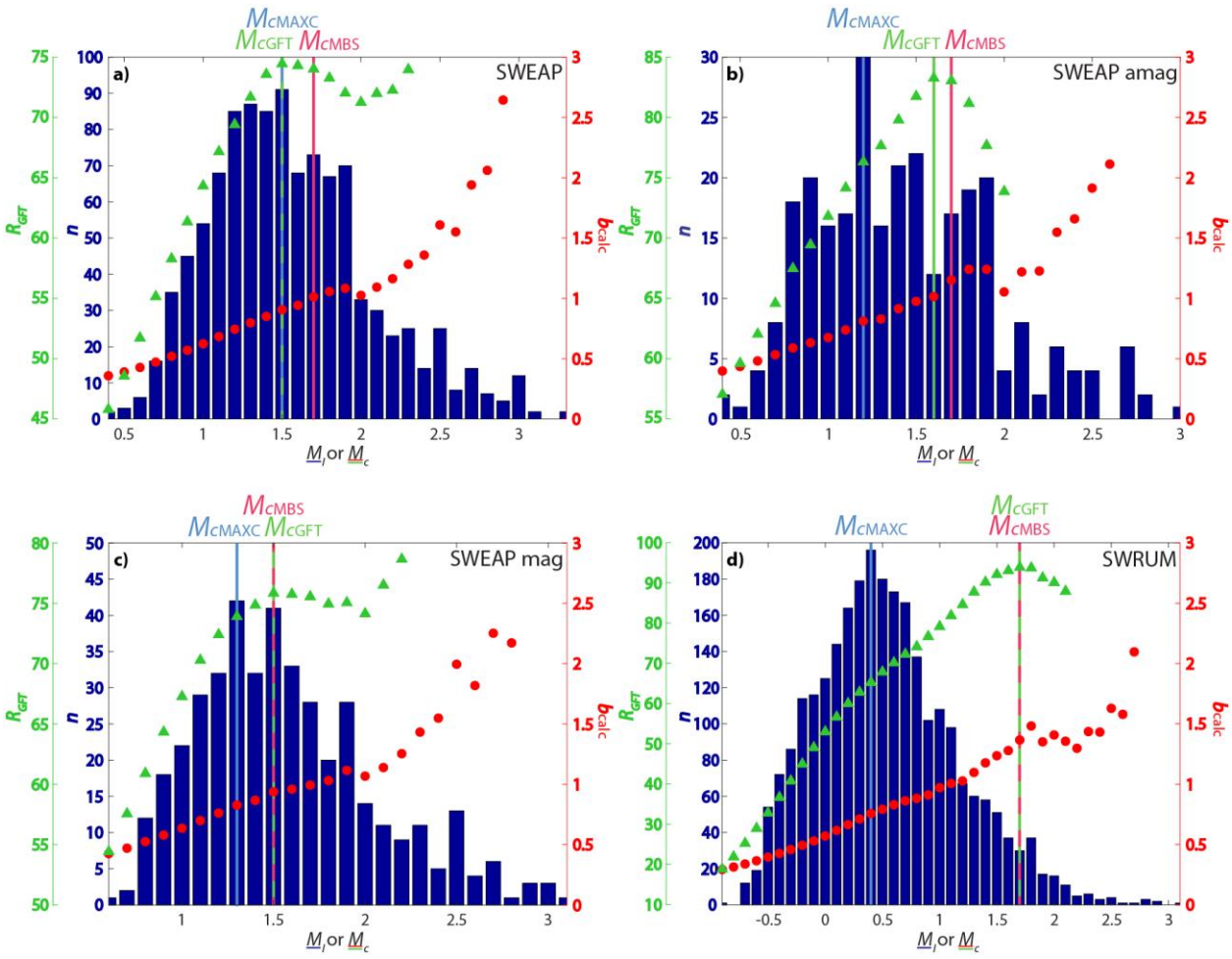

Figure 5. Graphical representations of $M_{c\mathrm{MAXC}}$, $M_{c\mathrm{GFT}}$ and $M_{c\mathrm{MBS}}$ estimates. Blue bars show the earthquake magnitude (M_l) distribution. $M_{c\mathrm{MAXC}}$ is the value of M_l for which most earthquakes have been recorded. Green triangles show the variations of R_{GFT} when varying M_c. The first maximum of this green curve gives the estimate of $M_{c\mathrm{GFT}}$. Red dots show the variations of b_{calc} (a value of b calculated based on M_c and the mean of magnitudes above M_c; see Appendix A) with M_c. $M_{c\mathrm{MBS}}$ is the first value of M_c for which the red curve reaches a plateau. Details about $M_{c\mathrm{MAXC}}$, $M_{c\mathrm{GFT}}$ and $M_{c\mathrm{MBS}}$ estimates are available in Appendix A.

The cut-off magnitudes (M_{co}) for all segments are well defined (Table 2 & Figure 6). The largest uncertainty is obtained for the complete SWEAP segment and can be explained by a slight change of slope of the cumulative distribution above magnitude 2.4 (Figure 6a). This change of slope is also observed, and even more pronounced, in the magmatic sub-segment (Figure 6c).

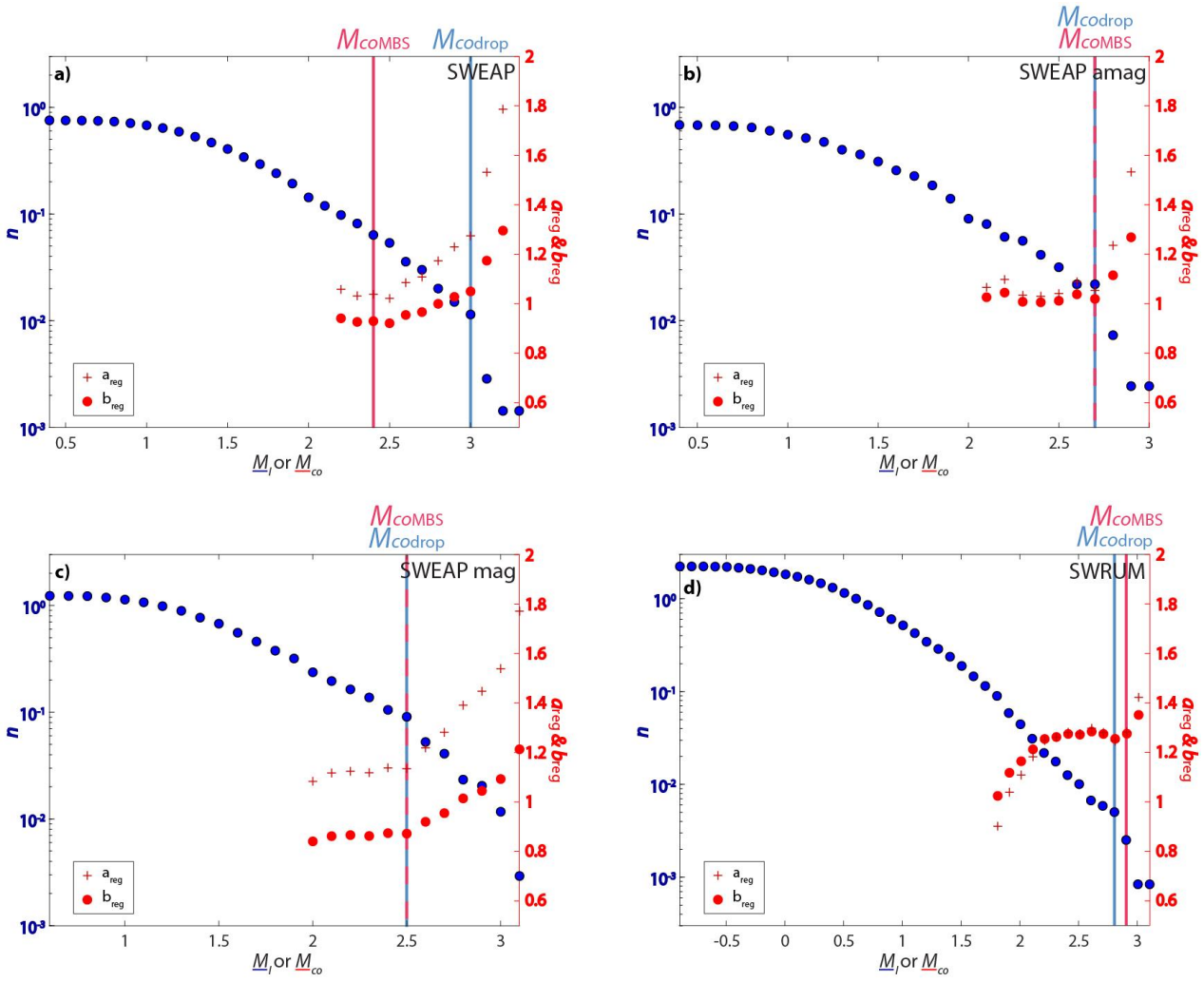

Figure 6. Graphical representations of $M_{co\mathrm{drop}}$ and $M_{co\mathrm{MBS}}$ estimates. Blue dots are cumulative distributions of the earthquakes magnitudes. $M_{co\mathrm{drop}}$ is the magnitude above which the distribution drops significantly. The red crosses and dots show the variations of a_{reg} and b_{reg} respectively (a- and b-values are obtained by regression between the previously estimated M_c and a varying M_{co}) with M_{co}. $M_{co\mathrm{MBS}}$ is the highest magnitude for which b_{reg} remains near the plateau value. Details about $M_{co\mathrm{drop}}$ and $M_{co\mathrm{MBS}}$ estimates are given in Appendix B.

For all ridge types, a-values are in the same range within error (Figure 7 & Table 2). This result indicates that the number of earthquakes along any ridge type is similar, only their magnitudes change depending on the thermal structure. The SWRUM segment possibly has a higher a-value which may be linked to the particularly active volcanic activity during the period of the recording (Schmid et al., 2017; Meier & Schlindwein, 2018). For the SWEAP region, the

371 *b*-values are close to 1 (Figure 7a-c & Table 2), as expected for oceanic ridges (e.g. Bayrak et al.,
372 2002). The value is the lowest (0.87±0.03) along the SWEAP magmatic portion. This portion is
373 thus the most likely to produce large magnitude events. The *b*-value for the complete SWEAP
374 segment is intermediate between the values obtained for the magmatic and amagmatic portions.
375 The highest value (1.26 ± 0.14) is obtained along the SWRUM axis (Figure 7d & Table 2). Such
376 a high value in a volcanic context is not surprising. The warm thermal regime prevents high
377 stress and seismicity is limited to low magnitude event.

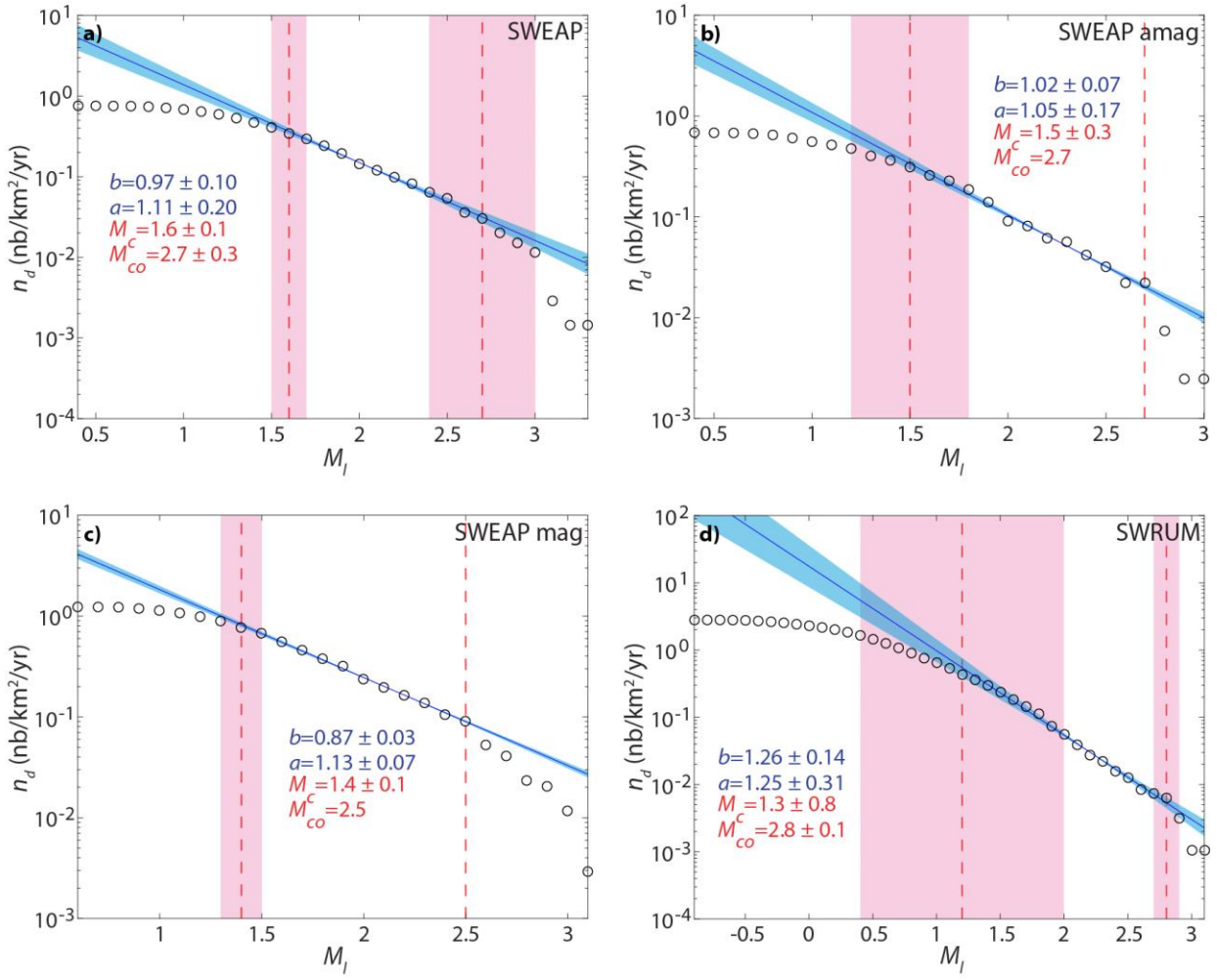

378
379 **Figure 7.** Cumulative density per seafloor surface area unit and per year (n_d) of earthquakes
380 magnitudes compared to regression of the Gutenberg-Richter law. Red dashed lines indicate the
381 location of M_c and M_{co} and red shaded zone shows their errors. The Gutenberg-Richter law
382 regression is represented by a blue line and shaded blue zone show the error on it due to the error
383 on M_c.

384 4.2. Volume of rock damaged by earthquakes

385 Before calculating the damaged volume, the magnitudes M_1 and M_2 introduced in equations
386 (1) and (2) need to be determined. While M_1 does not have much influence on the result as long
387 as it is small, M_2 has a significant influence as the largest earthquakes produce a relatively large
388 fraction of the total damage volumes. M_1 is obtained from the smallest magnitude recorded: 0.4
389 for the SWEAP regions and -0.9 for the SWRUM region. M_2 is estimated from the largest
390 teleseismic events recorded in each area: 5.8 for the SWEAP regions and 5.5 for the SWRUM
391 region. Teleseismic events reflect seismic activity over longer time intervals (around 20 years in
392 our case), which is more representative of the seismic activity of large events. Since it is highly
393 unlikely that the largest events in the study areas occurred in the last 20 years, our estimates are
394 lower bound values.

Ridge		M_1	M_2	Damaged volume per My in a lithospheric column (10^{-6} km/yr)	+/-	Damaged volume per My (%/My)	+/-	Damaged volume out of seismic zone (%)	+/-
SWEAP	Total	0.4	5.8	6.8	6.7	75	74	193	191
					3.4		37		96
	Amagmatic section	0.4	5.8	3.3	2.3	42	28	107	72
					1.3		17		43
	Magmatic section	0.4	5.8	20.6	5.8	206	58	527	148
					4.5		45		116
SWRUM		-0.9	5.5	0.80	0.6	6.7	5.0	9.8	7.3
					0.3		2.8		4.2

395
396

397 **Table 3.** Results of calculated damaged volume. In the error columns (+/-), for each ridge
398 portion, the upper line is the positive error and the lower line is the negative error.

399 The estimated damage-volumes from equation (2) are given in Table 3. Due to the
400 normalization of the earthquake distributions by the seafloor area and acquisition time (that
401 allows comparison of different mid-oceanic ridge portions), results are given in km/yr
402 ($km^3/km^2/yr$). The values quantify damaged lithospheric volumes per year for one km^2 surface
403 area of seismically active sea floor. They represent the height of lithosphere damaged each year
404 in a lithospheric column. The results are also given as a percentage of lithospheric volume
405 affected by earthquake damage after one million year of seismic activity, and after the entire
406 period the rock column will spend in the seismic zone of the rift valley given the observed
407 spreading rate and width of the valley. The estimated values do not account for possible
408 reactivation of fault zones or damage volume overlap, so some of the presented results are over

100% (see discussion below). Errors are calculated by computing the damaged volume for all the possible *a* and *b* values within their errors (with a resolution of 0.01). The results obtained follow a lognormal distribution. This is because *a* and *b* occur as exponents in equation (2). A consequence of this is that errors should be asymmetrical. Errors are obtained as follows:

$$\Delta V_{RD+} = 10^{\log_{10}(V_{RD}(a,b))+\mathrm{std}(\log_{10}(V_{RD\mathrm{list}}))} - V_{RD}(a,b) \quad (3)$$

$$\Delta V_{RD-} = V_{RD}(a,b) - 10^{\log_{10}(V_{RD}(a,b))-\mathrm{std}(\log_{10}(V_{RD\mathrm{list}}))} \quad (4)$$

with ΔV_{RD+} and ΔV_{RD-} representing the positive and negative error on V_{RD}, respectively; $V_{RD\mathrm{list}}$ is the list of damage volumes obtained from varying *a* and *b* within their errors; std is the standard deviation.

The most striking result is the significant portion of damaged rock along the magmatic and amagmatic segments compared to the volcanic one. While more than half of the seismic zone volume is damaged along the SWEAP region after one million year, only a few percent of the seismic zone is damaged along the SWRUM region. For the SWEAP portions, the amagmatic section shows the least damage with $42 \pm {}^{28}_{17}\%$ of rock volume damaged after one million year in the seismic zone and $107 \pm {}^{72}_{43}\%$ after the rock volume has been brought out of the seismic zone by the ridge spreading. The most damaged section is the magmatic section, consistent with the more frequent occurrence of large earthquakes, inducing large damage volumes. The damage volumes are well over 100% after only one million year. The complete SWEAP segment returns volumes intermediate between the magmatic and amagmatic segments with $75 \pm {}^{74}_{37}\%$ of damaged volume after one million year and $193 \pm {}^{191}_{96}\%$ damaged volume once the rock volume is out of the seismic zone.

5. Discussion

5.1. Fault reactivation, damage zone overlaps and volume damage

Several observations indicate that fault reactivation has limited effects on the estimated damaged volume. Firstly, the distribution of earthquakes in the seismic zones is pervasive and does not show the characteristic alignments typical of large faults (Figures 1 & 3). Secondly, the estimated focal mechanisms in the SWEAP segment have a high degree of variation, indicative of a complex stress field and strain partitioning (Schmid & Schlindwein, 2016). Finally,

clustered seismicity is very limited and earthquakes with similar waveforms represent less than 10% of the recorded seismicity.

In contrast, damage zone overlap is likely to have a major contribution when the damage volume becomes an important portion of the seismic zone and is likely responsible for the calculated damage volumes exceeding 100% along the SWEAP segment. Because the damage volume of an earthquake increases exponentially with its magnitude (equation (2)) and the probability of one earthquake to produce damage overlapping previously damaged rock is proportional to the size of its damage zone, this contribution increases with the proportion of large magnitude earthquakes. Damage volumes exceeding 100% are thus indicative of a significant portion of the lithosphere being damaged several times, most likely leading to large scale connected permeability.

5.2. Earthquakes depth and volume damage

In this section we compare our results to the earthquakes distribution obtained by Grevemeyer et al. (2019). The main difference between the two datasets are the location and more particularly the depth of the earthquakes. Unfortunately, they did not calculate earthquake magnitudes, so we cannot compare this parameter with our results. Our deepest seismic activity is located around 20 km, while theirs is located around 16 km depth. If most of the seismicity is concentrated in a 20 km wide undulating band as in our case, Grevemeyer et al.'s (2019) relocation also shows some shallow seismic activity between 1-4 km depth in the west part of the segment. All maps and earthquakes distribution histograms for the Grevemeyer et al. (2019) data are available in the Supplementary Materials.

We assume the *a*- and *b*-values are the same as the one we calculate with our dataset. This implies that the damage calculation we use returns the same results given in km/yr. However, the size of the seismic zone has an impact on the damaged volume percentages. As the width and the length of the studied section are the same, the difference involves the thickness of the seismic zone. The thinner the zone, the denser the seismic activity and the higher the percentages, but the absolute depth has no impact. The thickness of the seismic zone of Grevemeyer et al. (2019) is ~8 km in the magmatic part and ~7 km in the amagmatic part (adding the thicknesses of shallow and deep seismic zones). Both these thickness are thinner than the ones estimated based on our dataset. This would result in higher damage volume percentages. Thus, regardless of the

earthquakes depth, our estimates point to substantial volume of rock damage, sufficient to enable water penetration and subsequent serpentinization down to the depth of the seismic zone. The absolute depth of the seismic zone then defines the thickness of the serpentinized layer.

5.3. Seismicity and serpentinization

Serpentinization leads to rock weakening (e.g. Escartin et al., 1997). However, weakening does not necessarily imply that the rock becomes aseismic. Experiments on serpentinites have shown that seismic response may arise when shearing takes place under sufficiently high stress (Reinen, 2000; Brantut et al., 2016). Large magnitude earthquakes have also been reported from serpentinized zones, particularly in subduction zones (e.g. Emry et al., 2014) and transform faults (e.g. Abercrombie & Ekström, 2001) where some of the highest magnitude earthquakes occur. However, it is important to distinguish between the different stress fields at subduction zones, transform faults, and mid-oceanic ridges. Mid-oceanic ridges experience purely extensional stresses, and it is well established that rocks are weaker and fracture more easily under tension (Sibson, 1998). Less stress can be accumulated within the rocks leading to lower magnitude seismicity.

Horning et al. (2018) presented a study of the microseismicity at the Rainbow Massif located along the Mid-Atlantic Ridge. The massif formed by exhumation of the lithosphere along a large, currently inactive, detachment fault. These authors concluded that serpentinization and associated reaction driven expansion is likely the main cause for the recorded seismic activity. All the seismic events at the Rainbow massif are of rather low magnitude, most of them below local magnitude 1.5 with an average around 0.5. These magnitudes are much smaller than the ones form our SWEAP catalogue. Our detection limit would be too high to record serpentinization-produced seismicity. This may explain the aseismic zone along the SWEAP segment.

Serpentinization was not the main process generating the recorded seismicity along the SWEAP segment. We infer that most of the seismicity takes place prior to serpentinization, in a zone where serpentine is not yet stable, but is subsequently transported towards the zone of serpentine stability during progressive ridge opening. This interpretation is supported by the Vp/Vs ratios (around 1.77) which are closer to what would be expected for a dry mantle rather than for serpentinized peridotite (Christensen, 2004). Also, our *b*-values are close to what is

497 expected for mid-oceanic ridges (Bayrak et al., 2002) and much lower than what is obtained for
498 serpentinized zones (e.g. 1.7 in Horning et al., 2018).
499 Hints of the presence of serpentine can be seen in the seismic data. The proportion of small
500 magnitude earthquakes seem to increase towards the aseismic zone above ~12 km depth for the
501 magmatic portion and above ~16 km depth for the amagmatic one (Figure 2d). This could
502 indicate the onset of serpentinization (a few percent) or the preferential uptake of part of the
503 stress by the weaker aseismic zone above. The focal mechanisms calculated from the
504 microseismicity are diverse and differ from the normal faulting shown by larger teleseismic
505 events (Schmid & Schlindwein, 2016). This observation may indicate that the far-field tectonic
506 stress is perturbed by local stresses possibly generated by volume changes associated with
507 serpentinization reactions. The higher *b*-value associated with the lower seismic activity of the
508 amagmatic SWEAP portion compared to the magmatic portion could indicate a more extensive
509 serpentinization in the amagmatic portion. It also seems unlikely that the colder amagmatic
510 lithosphere would produce less and lower magnitude seismic activity than a warmer one under a
511 similar stress field.

512 5.4. Three types of ultra-slow ridge sections

513 Our study considers three types of ultra-slow ridge regimes: amagmatic, magmatic and
514 volcanic (Figure 8). These ridge types are characterized by distinctive seismic activities and
515 seismic zone shapes, thus distinctive volumes of damaged rocks (Table 3). This result leads to
516 pronounced variations in the extent of expected serpentinization. In the following, we present
517 models for the interaction between serpentinization and seismic activity for each ridge type. The
518 position of the isotherms in Figure 8 is solely based on the position of the BDTZ and the
519 assumption of a linear thermal gradient towards the seafloor. It does not take into account
520 complexities due to magmatic intrusions or hydrothermal activity.
521 The amagmatic ridge type (Figure 8a) is characterized by a low thermal gradient and a deep
522 BDTZ in the axial valley (~20 km depth in our case). The lack of magmatic activity results in
523 almost no thermal uplift at the ridge axis and in a very thin and discontinuous basaltic crust.
524 Oceanic extension is taken up by tectonics with continuous exhumation of mantle rocks by
525 flexural rotation along large detachment faults (Sauter et al., 2013) leading to an unusually
526 smooth seafloor (Cannat et al., 2006). The seismic zone forms a deep, ~7 km thick band that

climbs somewhat away from the ridge axis on one side to reach its shallowest depth (Figure 1d). Referring to Sauter et al. (2013) flip-flop model of exhumation, the shallowest seismicity could be linked to limited magmatic activity close to the active detachment. The percentage of damage after the rock volume is brought out of the seismic zone by the ridge spreading is around 100% (Table 3). Even considering that part of this is overlapping damage, it seems reasonable to assume that a connected network of fractures is created by the seismicity. This would be in agreement with the serpentinization model presented by Rouméjon et al. (2015) based on dredged peridotites from the SWIR. This model suggests that serpentinization is concentrated within high-permeability corridors possibly produced by tectonic activity. Seawater can then easily penetrate into the peridotite, leading to partial serpentinization of the mantle down to the limit of serpentine stability around the 400-500˚C isotherm. The supply of water is not limited and the serpentinization front is thermally controlled. This is consistent with the presence of the aseismic zone, weak seismicity of the amagmatic portion, and lower magnitudes towards the aseismic zone.

The magmatic ridge type (Figure 8b) has steeper thermal gradients with its BDTZ slightly shallower than the amagmatic type (~17 km depth in our case). Its magmatic activity leads to the formation of a thin almost continuous basaltic crust on the seafloor. Most of the spreading is accommodated by tectonics with the development of some large detachment faults, but magmatic intrusions also play a significant role. This mode of ridge opening is comparable to what is observed at segment ends along slow ridges (e.g. the Mid-Atlantic Ridge). Similarly to the amagmatic section, the base of the seismic zone becomes shallower on one side. However, the seismic zone has a triangular cross-section that climbs above the assumed 400-500˚C isotherm in the axial valley (Figure 1e). This shape is probably linked to the magmatic activity of the ridge. As the basaltic crust is thin and the damage volumes exceeds 100% already after one million year, indicating that connected fault network is formed very quickly, water should be able to penetrate pervasively from the seafloor towards the serpentinization front. The maximum serpentinization depth away from the thermal influence of the ridge axis should thus correspond to the lower limit of the seismic zone. However, in this case a substantial part of the damaged rock volume may represent hydrothermally altered gabbro that is not converted into serpentinite. The pervasive water infiltration leading to the alteration of the lithosphere within the thermal stability field of serpentine is consistent with the occurrence of an aseismic zone.

Seismic activity is more intense than expected. Indeed, the environment being warmer than the amagmatic segment would lead to weaker rock. As an aseismic zone is present similarly to the amagmatic context, leading to a similar profile, we would expect similar to lower seismic activity than for the amagmatic ridge type. This supplement of seismic activity could be the consequence of the magmatic activity. The intrusion of magmatic bodies and dykes could generate a supplementary source of stress coming from below and that consequently cannot be accommodated by the upper altered lithosphere. This stress would generate the supplementary seismicity. This would mean that some magmatic activity would favor fracturation and fluids circulation into the upper lithosphere.

The volcanic ridge type (Figure 8c) is influenced by the proximity to a major volcanic center. Thermal gradients are the steepest of the three ridge types and magmatism becomes the dominant spreading mechanism. In a cross-section perpendicular to the ridge axis the seismic zone has an inversed V-shape (Figure 3d). Basalt intrusions into the lithosphere produce additional seismicity. Damage due to seismicity is distributed within the lithosphere above the BDTZ (Figure 4d). However, permeability generation by seismic damage is very limited. In addition, the thick magmatic crust prevents seawater to efficiently reach the underlying mantle. Serpentinization is thus limited to localized fault zones that cut through the thick crust and is expected to be most common away from the ridge axis once the lithosphere has cooled. However, significant hydrothermal activity has been identified associated with volcanic centers (Michael et al. 2003; Edmonds et al. 2003) and tremor activity attributed to enhanced hydrothermal activity has been recorded along the SWRUM segment (Meier and Schlindwein, 2018), suggesting that water supply for serpentinization may also be promoted by other mechanisms than the ones considered in the present study.

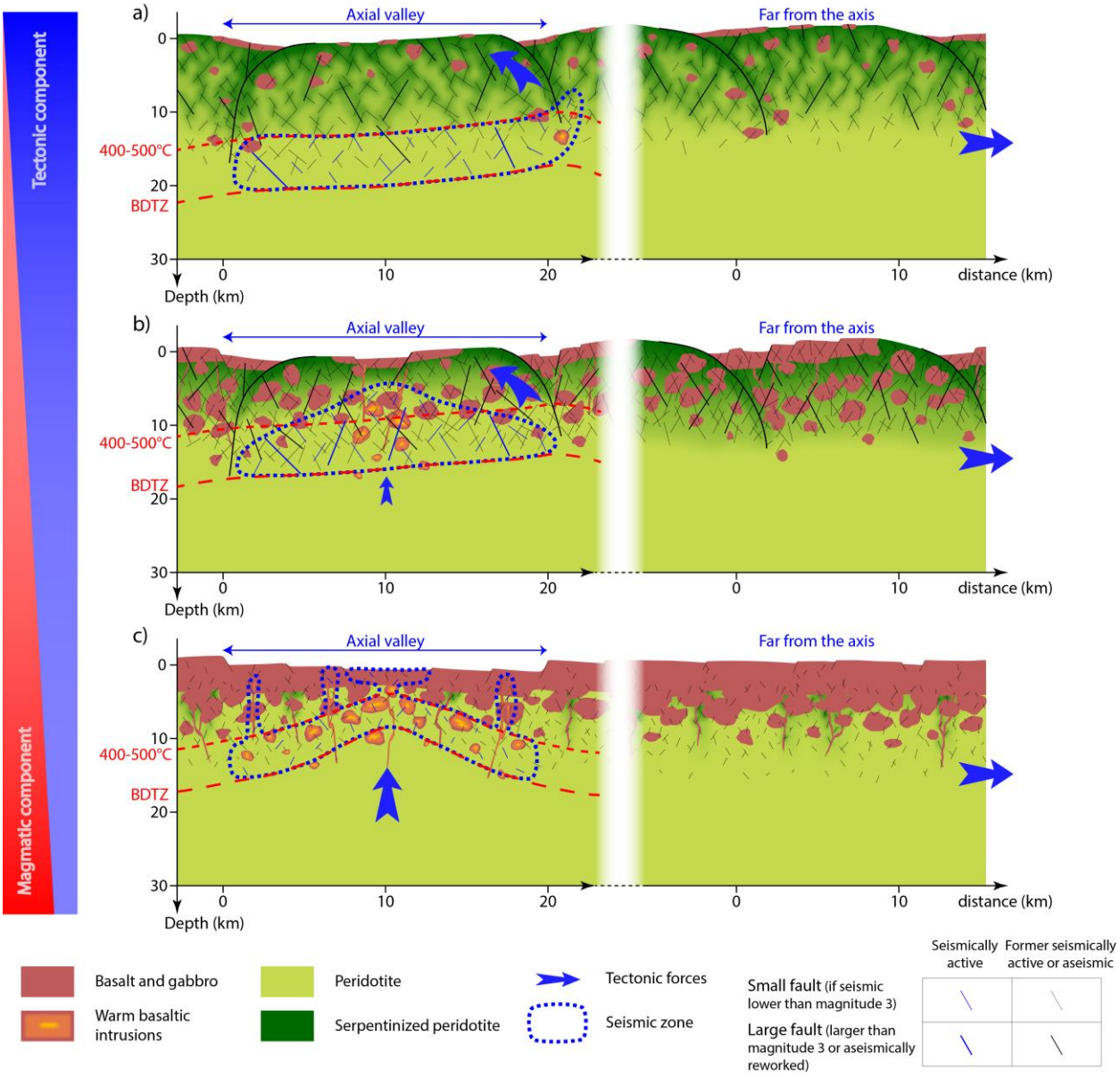

Figure 8. Conceptual sketch for the evolution of fracturing and subsequent serpentinization with distance to the ridge for the different ultra-slow ridge types. a) The amagmatic ridge type shows corridors of preferential serpentinization. b) The magmatic ridge type shows extensive fracturing, allowing pervasive serpentinization. c) The volcanic ridge type shows limited earthquake-produced serpentinization. Isotherms have been determined at the ridge axis from the position of the brittle-ductile transition zone and assuming a linear gradient to the seafloor surface. The right side of the sub-figures shows the lithosphere after the ridge extension has brought it away from the ridge axis and the temperature does not limit the extent of serpentinization anymore.

5.5. Volume of serpentinization along mid-oceanic ridges

Gutenberg-Richter *b*-values have a tendency to increase with ridge spreading rates (Bayrak et al., 2002) and the associated increase in magmatic activity. Along the Mid-Atlantic Ridge, classified as a slow ridge (spreading rates below 55 mm/yr), the magmatically active segment centers, have been reported to have higher *b*-values than the more tectonically active segment ends (Kong et al., 1992; Grevemeyer et al., 2013). The *b*-values of slow ridges segment centers are close to the *b*-values of our volcanic segment, while the *b*-values of slow ridges segment ends are closer to the *b*-values of our magmatic segment. The magmatic ridge segment we describe in this paper can be assimilated with the less tectonically active portions of the slow-ridges. Ultra-slow and very-slow ridges (spreading rates below 20 mm/yr) represent around 20% of the world oceanic ridge system and produce around 5.5% of the seafloor, i.e., approximately 0.17 km^2/yr (Solomon, 1989). Slow ridges represent another 40 % of the ridges and produce 26% of the seafloor, i.e., approximately 0.77 km^2/yr.

Assuming that the SWIR is representative for all ultra-slow and very-slow ridges, we can estimate a global rate of serpentinization and associated water consumption. Major volcanic centers along ultra-slow ridges are spaced between 100 and 200 km apart (Sauter and Cannat 2010). A volcano's influence on magmatic activity typically extends to a 60 km radius (Sauter et al. 2004) including both magmatic and volcanic ridge types. The SWRUM segment is approximately 90 km long. We assume that this length corresponds to the mean length of the volcanic ridge type and that volcanic centers are located 150 kilometers apart. Each 150 km long section is then composed of 90 km volcanic ridge type, 30 km of magmatic ridge type and 30 km of amagmatic ridge type. Asymmetric spreading associated with less magmatic portions of slow ridges has been reported for approximately half of the slow ridges length (Escartin et al., 2008). Thus, the magmatic ridge type would correspond to half the slow ridges length.

We assume that serpentinization at the magmatic and amagmatic ridge types reaches ~13 km depth for the SWEAP segment, while the volcanic ridge type produces no serpentinization. Seismic reflection on another amagmatic segment of the SWIR, located close to the SWRUM segment showed that the seismic crust (including serpentinized mantle and gabbroic crust) is no more than 6 km thick (Momoh et al., 2017). There is thus a 7 km difference between the two estimates. This difference could be due to the environment of both experiments, the SWEAP segment being one of the slowest end-member of the ultra-slow spreading ridges while the

vicinity of the SWRUM segment has faster opening rates and likely slightly warmer regime leading to less deep serpentinization. In order to account for the fact that the SWEAP segment is in consequence not representative for most of the warmer ridges we make a compromise between our maximum serpentinization thickness and the one given by Momoh et al. (2017) by assuming that serpentinization reaches 9 km depth. This serpentinized layer comprises, in the case of the magmatic ridge type, an unknown proportion of gabbroic intrusions. Tucholke et al. (2008) modeled the changes in ridge spreading modes depending on the proportion of tectonic versus magmatic extension. The transition from an equivalent of our volcanic ridge type to an equivalent of our magmatic ridge type happens when the magmatism takes up less than 50% of the ridge spreading. This give us an estimate for the maximum fraction of gabbro (~50%) for the magmatic ridge type. We conservatively divide the serpentinized mantle thickness by two for the magmatic ridge type to take the content of gabbro into account.

The estimated total volume affected by serpentinization (whatever the extent) each year is then 2.2 km^3. Considering a linear gradient of serpentinization with depth we obtain a global serpentinization rate for ultra-slow to slow ridges of 1.1 km^3/yr. This estimate is approximately five times the estimate made by Cannat et al. (2010). Abyssal peridotites contain 10-15 % H_2O (Mével, 2003). Hence, our results indicate that earthquake-assisted serpentinization processes store 0.11 to 0.17 km^3 of water per year along ultra-slow to slow ridges. A lower bound estimate can be obtained if we take into account that the volume we consider is aseismic, indicating a serpentinization of at least 10% of the total volume (Escartin et al., 2001). This leads to a serpentinization rate of 0.22 km^3/yr. This estimate is of the same order as the one given by Cannat et al. (2010) and corresponds to a water volume of 0.02 to 0.03 km^3/yr.

6. Conclusions

Three types of ultra-slow ridge sections: amagmatic, magmatic, and volcanic are associated with different thermal and tectonic regimes. Based on the recorded seismic activity, the damage volumes of rocks estimated for magmatic and amagmatic ridge types indicate that seismicity creates significant pathways for water to migrate as deep as the limit of stability of serpentine, implying that serpentinization can be sustained down to these depths. The occurrence of some magmatic activity seems to favor the creation of a fracture network and pervasive serpentinization, it however implies the presence of significant volumes of gabbroic intrusions in

652 the upper lithosphere. In the volcanic sections, the seismically-damaged volume is limited to a
653 few percent due to a higher thermal gradient. This results in limited earthquake-related
654 serpentinization in the proximity of volcanic centers. Along slow and ultra-slow ridges, we
655 calculate that between 0.02 and 0.17 km^3 per year of water is consumed and stored in
656 serpentinized oceanic lithosphere. This value is up to five times higher than what has been
657 previously estimated indicating that the water storage potential of the slow ridges and ultra-slow
658 ridges may be higher than hitherto thought.

659 **Appendix A: Earthquake catalogue completeness magnitude M_c**

660 The maximum curvature (MAXC) method chooses $M_{c\mathrm{MAXC}}$ as the most frequent earthquake
661 magnitude (Wyss et al., 1999). This method has a tendency to underestimate the magnitude of
662 completeness, M_c.

663 The Goodness-of-Fit Test (GFT) involves fitting the Gutenberg-Richter law by using
664 different values of M_c and keeping the one for which the fit is the best ($M_{c\mathrm{GFT}}$). The best fit is
665 determined by maximizing a value R_{GFT} (Wiemer & Wyss, 2000):

666 $$R_{GFT}(a_{\mathrm{fit}}, b_{\mathrm{fit}}, M_{c\mathrm{var}}) = 1 - \frac{\sum_{i=i_{M_{c\mathrm{var}}}}^{N} \left| n(M(i)) - 10^{a_{\mathrm{fit}} - b_{\mathrm{fit}} M(i)} \right|}{\sum_{i=1}^{N} n(M(i))}, \qquad \text{(A.1)}$$

667 where $i_{M_{c\mathrm{var}}}$ is the index associated with the varying magnitude of completeness, $M_{c\mathrm{var}}$, in
668 the earthquakes cumulative distribution. a_{fit} and b_{fit} are the Gutenberg-Richter parameters
669 obtained by fitting the earthquake cumulative distribution between $M_{c\mathrm{var}}$ and the maximum
670 recorded magnitude. If there are several maxima of R_{GFT}, the one at smallest magnitude is used
671 to determine $M_{c\mathrm{GFT}}$.

672 Estimating M_c by *b*-value stability (MBS) involves plotting *b*-values obtained by varying M_c
673 and keeping $M_{c\mathrm{MBS}}$ as the smallest M_c for which the *b*-values reach a plateau (Woessner &
674 Wiemer, 2005). *b* is calculated based on the varying $M_{c\mathrm{var}}$, the mean magnitude of events of
675 magnitude larger than $M_{c\mathrm{var}}$ ($\langle M \rangle$), and the bin size used for the distribution (ΔM) (Marzocchi &
676 Sandri, 2003) taken as 0.1 for our data.

677 $$b_{\mathrm{calc}}(M_{c\mathrm{var}}) = \frac{\log_{10}(\exp(1))}{\langle M \rangle - (M_{c\mathrm{var}} - \Delta M/2)} \qquad \text{(A.2)}$$

678 To identify when b_{calc}-values reach a plateau in a $M_{c\mathrm{var}}$ vs b_{calc} plot we use the *b*-value
679 uncertainty (δb) proposed by Shi and Bolt (1982):

$$\delta b = 2.3 b_{\mathrm{calc}}{}^2 \sqrt{\frac{\sum_{i=1}^{n_{\mathrm{tot}}} (M_i - \langle M \rangle_{\mathrm{tot}})^2}{n_{\mathrm{tot}} \cdot (n_{\mathrm{tot}} - 1)}} \qquad \text{(A.3)}$$

In this equation, the magnitude of individual events, M_i, as well as the mean magnitude of all earthquakes, $\langle M \rangle_{\mathrm{tot}}$, are used. n_{tot} is the total number of events. The plateau is reached if the variations of b_{calc} over a certain number of values (k) stay smaller than the criterion δb:

$$\Delta b = |b_{\mathrm{ave}} - b_{\mathrm{calc}}| \leq \delta b \qquad \text{(A.4)}$$

$$\text{with } b_{\mathrm{ave}} = \frac{\sum_{i=0}^{k} b_{\mathrm{calc}}(M_{c\mathrm{var}} + \Delta M \cdot i)}{k+1}$$

The derived b_{ave} is the average b_{calc}-value calculated over (k+1) values (Woessner & Wiemer, 2005). Our datasets span a limited range of magnitudes leading to quite short plateaus (when possible to identify). Hence, we used a value k=3, smaller than the value of 5 recommended by Woessner & Wiemer (2005). This method has a tendency to give higher (conservative) values of M_c than the two other methods.

Appendix B: Earthquake catalogue cut-off magnitude M_{co}

The method to estimate the $M_{co\mathrm{drop}}$ is based on the fact that points from the cumulative distribution should be binned with a regular spacing in semi-logarithmic space and follow a linear trend (the Gutenberg-Richter law). The magnitude $M_{co\mathrm{drop}}$ is estimated as the magnitude above which a significant decrease in the number of earthquakes recorded happens. We first calculate the list of differences between two consecutive magnitudes from the logarithm of the cumulative distribution. From this list, we extract its median and standard deviation only using differences obtained for magnitudes above the previously estimated M_c. The use of the median over the mean is best to avoid the influence of the points with a large difference as these are the ones we want to exclude. $M_{co\mathrm{drop}}$ is determined as the highest magnitude beyond which the difference between two consecutive magnitudes in the cumulative distribution exceeds the median value plus the standard deviation.

The estimation of $M_{co\mathrm{MBS}}$ follows a method similar to the estimate of $M_{c\mathrm{MBS}}$ but relying on a b-value obtained from a regression (b_{reg}) instead of a calculation (b_{calc}; A.2). For decreasing M_{co}, a_{reg} and b_{reg} are obtained from a linear regression on the logarithm of the earthquakes cumulative distribution between previously estimated M_c and varying $M_{co\mathrm{var}}$. $M_{co\mathrm{MBS}}$ is estimated as the largest magnitude for which b_{reg} (and a_{reg}) reaches a plateau. To identify the

plateau, a value b_{ave} is calculated as the average of b_{reg} obtained for a certain number (k) of values of M_{covar}. The plateau is reached if the difference (Δb) between b_{reg} and b_{ave} is smaller than the standard deviation of the b_{reg} values used to calculate b_{ave}:

$$\Delta b = |b_{\mathrm{ave}} - b_{\mathrm{calc}}| \leq \delta b \qquad \text{(B.1)}$$

$$\text{with } b_{\mathrm{ave}} = \frac{\sum_{i=0}^{k} b_{\mathrm{reg}}(M_{covar} - \Delta M \cdot i)}{k+1} \text{ and } \delta b = \mathrm{std}(b_{\mathrm{reg}}(M_{covar} - \Delta M \cdot i), i = 0 \text{ to } k)$$

ΔM is the bin size used for the distribution. In this study we used k=4.

Acknowledgments

This project has been supported by the European Union's Horizon 2020 Research and Innovation Programme [ERC Advanced Grant Agreement n°669972, 'Disequilibirum Metamorphism' ('DIME'), to B. Jamtveit]. Seismic data acquisition was supported by the German Science Foundation [grants SCHL853/1-1 and SCHL853/3-1 to V. Schlindwein]. Instruments were provided by the AWI DEPAS OBS pool. The authors acknowledge the efforts of the crews of RV Polarstern cruises ANT-XXIX/2+8 and ARK-XXIV/3, RV Meteor cruise M101 and RV Marion Dufresne during the OBS operations. We thank Ingo Grevemeyer for the kind sharing of his relocation data. The lists of hypocenters (including locations and magnitudes) and MatLab files used for estimating *a*- and *b*- values and damaged volumes calculation are available at: https://osf.io/zt23n/.

References

Abercrombie, R. E., & Ekström, G. (2001). Earthquake slip on oceanic transform faults. *Nature*, *410*, 74-77. https://doi.org/10.1038/35065064

Bach, W., Paulick, H., Garrido, C. J., Ildefonse, B., Meurer, W. P., & Humphris, S. E. (2006). Unraveling the sequence of serpentinization reactions: Petrography, mineral chemistry, and petrophysics of serpentinites from MAR 15°N (ODP Leg 209, Site 1274). *Geophysical Research Letters*, *33*(13). https://doi.org/10.1029/2006GL025681

Barnes, J. D., Paulick, H., Sharp, Z. D., Bach, W., & Beaudoin, G. (2009). Stable isotope (δ18O, δD, δ37Cl) evidence for multiple fluid histories in mid-Atlantic abyssal peridotites (ODP Leg 209). *Lithos*, *110*(1-4), 83-94. https://doi.org/10.1016/j.lithos.2008.12.004

Bayrak, Y., Yılmaztürk, A., & Öztürk, S. (2002). Lateral variations of the modal (a/b) values for the different regions of the world. *Journal of Geodynamics*, *34*(5), 653–666. https://doi.org/10.1016/S0264-3707(02)00037-6

Ben-Zion, Y. (2008). Collective behavior of earthquakes and faults: continuum-discrete transitions, progressive evolutionary changes, and different dynamic regimes. *Reviews of Geophysics*, *46*(4). https://doi.org/10.1029/2008RG000260

Ben-Zion, Y., & Zhu, L. (2002). Potency-magnitude scaling relations for southern California earthquakes with 1.0<ML<7.0. *Geophysical Journal International*, *148*(3), F1–F5. https://doi.org/10.1046/j.1365-246X.2002.01637.x¨

Brantut, N., Passelègue, F. X., Deldicque, D., Rouzaud, J.-N., Schubnel, A. (2016). Dynamic weakening and amorphization in serpentinite during laboratory earthquakes. *Geology*, *44*(8), 607-610. https://doi.org/10.1130/G37932.1

Cannat, M., Fontaine, F., & Escartín, J. (2010). Serpentinization and associated hydrogen and methane fluxes at slow spreading ridges. In P. A., Rona, C. W., Devey, J., Dyment, B. J., Murton (Eds.), *Diversity Of Hydrothermal Systems On Slow Spreading Ocean Ridges* (Vol. 188, pp. 241–264). Washington, D. C.: American Geophysical Union. https://doi.org/10.1029/2008GM000760

Cannat, M., Sauter, D., Mendel, V., Ruellan, E., Okino, K., Escartin, J., Combier, V., & Baala, M. (2006). Modes of seafloor generation at a melt-poor ultraslow-spreading ridge. *Geology*, *34*(7), 605–608. https://doi.org/10.1130/G22486.1

Christensen, N. I. (2004). Serpentinites, Peridotites, and Seismology. *International Geology Review*, *46*(9), 795-816. https://doi.org/10.2747/0020-6814.46.9.795

Delescluse, M., & Chamot-Rooke, N. (2008). Serpentinization pulse in the actively deforming central Indian basin. *Earth and Planetary Science Letters*, *276*(1-2), 140–151. https://doi.org/10.1016/j.epsl.2008.09.017

DeMets, C., Gordon, R. G., Argus, D. F., & Stein, S. (1990). Current plate motions. *Geophysical Journal International*, *101*(2), 425–478. https://doi.org/10.1111/j.1365-246X.1990.tb06579.x

DeMets, C., Gordon, R. G., Argus, D. F., & Stein, S. (1994). Effect of recent revisions to the geomagnetic reversal time scale on estimates of current plate motions. *Geophysical Research Letters*, *21*(20), 2191–2194. https://doi.org/10.1029/94GL02118

766 Dick, H. J. B., Jian Lin, J. B., & Schouten, H. (2003). An ultraslow-spreading class of ocean
767 ridge. *Nature*, *426*, 405–412. https://doi.org/10.1038/nature02128
768 Edmonds, H. N., Michael, P. J., Baker, E. T., Connelly, D. P., Snow, J. E., Langmuir, C. H.,
769 Dick, H. J. B., Mühe, R., German, C. R., & Graham, D. W. (2003). Discovery of abundant
770 hydrothermal venting on the ultraslow-spreading Gakkel ridge in the Arctic Ocean. *Nature*, *421*,
771 252–256. https://doi.org/10.1038/nature01351
772 Edwards, B., Allmann, B., Fäh, D., & Clinton, J. (2010). Automatic computation of moment
773 magnitudes for small earthquakes and the scaling of local to moment magnitude. *Geophysical*
774 *Journal International*, *183*(1), 407–420. https://doi.org/10.1111/j.1365-246X.2010.04743.x
775 Emry, E. L., Wiens, D. A., & Garcia-Castellanos, D. (2014). Faulting within the Pacific
776 plate at the Mariana Trench: Implications for plate interface coupling and subduction of hydrous
777 minerals. *Journal of Geophysical Research: Solid Earth*, *119*, 3076-3095.
778 https://doi.org/10.1002/2013JB010718
779 Escartin, J., Hirth, G., & Evans, B. (1997). Effects of serpentinization on the lithospheric
780 strength and the style of normal faulting at slow-spreading ridges. *Earth and Planetary Science*
781 *Letters*, *151*(3-4), 181-189. https://doi.org/10.1016/S0012-821X(97)81847-X
782 Escartin, J., Hirth, G., & Evans B. (2001). Strength of slightly serpentinized peridotites:
783 Implications for the tectonics of oceanic lithosphere. *Geology*, *29*(11), 1023–1026.
784 https://doi.org/10.1130/0091-7613(2001)029<1023:SOSSPI>2.0.CO;2
785 Escartin, J., Smith, D. K., Cann, J., Schouten, H., Langmuir, C. H., & Escrig, S. (2008).
786 Central role of detachment faults in accretion of slow-spreading oceanic lithosphere. *Nature*,
787 *455*, 790-794. https://doi.org/10.1038/nature07333
788 Font, Y., Kao, H., Lallemand, S., Liu, C.-S., & Chiao, L.-Y. (2004). Hypocentral
789 determination offshore Eastern Taiwan using the Maximum Intersection method. *Geophysical*
790 *Journal International*, *158*(2), 655-675. https://doi.org/10.1111/j.1365-246X.2004.02317.x
791 Grevemeyer, I., Reston, T. J., & Moeller, S. (2013). Microseismicity of the Mid-Atlantic
792 Ridge at 7°S–8°15′S and at the Logatchev Massif oceanic core complex at 14°40′N–14°50′N.
793 *Geochemistry, Geophysics, Geosystems*, *14*, 3532-3554. https://doi.org/10.1002/ggge.20197
794 Grevemeyer, I., Hayman, N. W., Lange, D., Peirce, C., Papenberg, C., Van Avendonk, H. J.
795 A., Schmid, F., Gómez de La Peña, L., & Dannowski, A. (2019). Constraining the maximum

depth of brittle deformation at slow- and ultraslow-spreading ridges using microseismicity. *Geology*, *47*(11), 1069-1073. https://doi.org/10.1130/G46577.1

Gutenberg, B., & Richter, C. F. (1944). Frequency of earthquakes in California. *Bulletin of the Seismological Society of America*, *34*(4), 185–188.

Harper, G. D. (1985). Tectonics of slow spreading mid-ocean ridges and consequences of a variable depth to the brittle/ductile transition. *Tectonics*, *4*(4), 395-409. https://doi.org/10.1029/TC004i004p00395

Holm, N. G. & Charlou, J. L. (2001). Initial indications of abiotic formation of hydrocarbons in the Rainbow ultramafic hydrothermal system, Mid-Atlantic ridge. *Earth and Planetary Science Letters*, *191*(1-2), 1–8. https://doi.org/10.1016/S0012-821X(01)00397-1

Horning, G., Sohn, R. A., Canales, J. P., & Dunn, R. A. (2018). Local seismicity of the Rainbow massif on the Mid-Atlantic ridge. *Journal of Geophysical Research: Solid Earth*, *123*(2), 1615–1630. https://doi.org/10.1002/2017JB015288

Hövelmann, J., Austrheim, H., & Jamtveit, B. (2012). Microstructure and porosity evolution during experimental carbonation of a natural peridotite. *Chemical Geology*, *334*, 254–265. https://doi.org/10.1016/j.chemgeo.2012.10.025

Husen, S., & Smith, R. B. (2004). Probabilistic earthquake relocation in three-dimensional velocity models for the Yellowstone National Park region, Wyoming. *Bulletin of the Seismological Society of America*, *94*(3), 880-896. https://doi.org/10.1785/0120030170

Jamtveit, B., Ben-Zion, Y., Renard, F., & Austrheim, H. (2018). Earthquake-induced transformation of the lower crust. *Nature*, *556*, 487–491. https://doi.org/10.1038/s41586-018-0045-y

Jamtveit, B., Malthe-Sørenssen, A., & Kostenko, O. (2008). Reaction enhanced permeability during retrogressive metamorphism. *Earth and Planetary Science Letters*, *267*(3-4), 620–627. https://doi.org/10.1016/j.epsl.2007.12.016

Kong, L. S. L., Solomon, S. C., & Purdy, G. M. (1992). Microearthquake Characteristics of a Mid-Ocean Ridge along-axis high. *Journal of Geophysical research: Solid Earth*, *97*(B2), 1659-1685. https://doi.org/10.1029/91JB02566

Lomax, A., Virieux, J., Volant, P., & Berge, C. (2000). Probabilistic earthquake location in 3D and layered models: Introduction of a Metropolis-Gibbs method and comparison with linear

locations. In C.H., Thurber, N., Rabinowitz (Eds.), *Advances in Seismic Event Location* (pp 101-134). Springer, Dordrecht. https://doi.org/10.1007/978-94-015-9536-0_5

MacDonald, A. H., & Fyfe, W. S. (1985). Rate of serpentinization in seafloor environments. *Tectonophysics*, *116*(1-2), 123–135. https://doi.org/10.1016/0040-1951(85)90225-2

Malvoisin, B. (2015). Mass transfer in the oceanic lithopshere : Serpentinization is not isochemical. *Earth and Planetary Science Letters*, *430*, 75-85. https://doi.org/10.1016/j.epsl.2015.07.043

Malvoisin, B., Brunet, F., Carlut, J., Rouméjon, S., & Cannat, M. (2012). Serpentinization of oceanic peridotites: 2. Kinetics and processes of San Carlos olivine hydrothermal alteration. *Journal of Geophysical Research: Solid Earth*, *117*(B4). https://doi.org/10.1029/2011JB008842

Martin, B., & Fyfe, W. S. (1970). Some experimental and theoretical observations on the kinetics of hydration reactions with particular reference to serpentinization. *Chemical Geology*, *6*, 185–202. https://doi.org/10.1016/0009-2541(70)90018-5

Marzocchi, W., & Sandri, L. (2003). A review and new insights on the estimation of the *b*-value and its uncertainty. *Annals of Geophysics*, *46*(6), 1271-1282.

Meier, M., & Schlindwein, V. (2018). First in situ seismic record of spreading events at the ultraslow spreading southwest Indian ridge. *Geophysical Research Letters*, *45*(19), 10 360-10 368. https://doi.org/10.1029/2018GL079928

Mével, C. (2003). Serpentinization of abyssal peridotites at mid-ocean ridges. *Comptes Rendus Geoscience*, *335*(10-11), 825–852. https://doi.org/10.1016/j.crte.2003.08.006

Michael, P. J., Langmuir, C. H., Dick, H. J. B., Snow, J. E., Goldstein, S. L., Graham, D. W., Lehnert, K., Kurras, G., Jokat, W., Mühe, R., & Edmonds, H. N. (2003). Magmatic and amagmatic seafloor generation at the ultraslow-spreading Gakkel ridge, Arctic Ocean. *Nature*, *423*, 956–961. https://doi.org/10.1038/nature01704

Momoh, E., Cannat, M., Watremez, L., Leroy, S., & Singh, S. C. (2017). Quasi-3D seismic reflection imaging and wide-angle velocity structure of nearly amagmatic oceanic lithosphere at the ultraslow-spreading southwest Indian ridge. *Journal of Geophysical research: Solid Earth*, *122*(12), 9511-9533. https://doi.org/10.1002/2017JB014754

Moore, D. E., Lockner, D. A., Tanaka, H., & Iwata, K. (2004). The Coefficient of Friction of Chrysotile Gouge at Seismogenic Depths. *International Geology Review*, *46*(5), 385-398. https://doi.org/10.2747/0020-6814.46.5.385

O'Hanley, D. S. (1992). Solution to the volume problem in serpentinization. *Geology*, *20*(8), 705–708. https://doi.org/10.1130/0091-7613(1992)020<0705:STTVPI>2.3.CO;2

Plümper, O., King, H. E., Geisler, T., Liu, Y., Pabst, S., Savov, I. P., Rost, D., & Zack, T. (2017). Subduction zone forearc serpentinites as incubators for deep microbial life. *Proceedings of the National Academy of Sciences of the United States of America*, *114*(17), 4324–4329. https://doi.org/10.1073/pnas.1612147114

Reinen, L. A. (2000). Seismic and aseismic slip indicators in serpentinite gouge. *Geology*, *28*(2), 135-138. https://doi.org/10.1130/0091-7613(2000)28<135:SAASII>2.0.CO;2

Rouméjon, S., & Cannat, M. (2014). Serpentinization of mantle-derived peridotites at mid-ocean ridges: Mesh texture development in the context of tectonic exhumation. *Geochemistry, Geophysics, Geosystems*, *15*(6), 2354–2379. https://doi.org/10.1002/2013GC005148

Rouméjon, S., Cannat, M., Agrinier, P., Godard, M., & Andreani, M. (2015). Serpentinization and Fluid Pathways in Tectonically Exhumed Peridotites from the Southwest Indian Ridge (62–65°E). *Journal of Petrology*, *56*(4), 703-734. https://doi.org/10.1093/petrology/egv014

Sauter, D., & Cannat, M. (2010). The ultraslow spreading southwest Indian ridge. In: P. A., Rona, C. W., Devey, J., Dyment, B. J., Murton (Eds.), *Diversity Of Hydrothermal Systems On Slow Spreading Ocean Ridges* (Vol. 188, pp. 153-173). Washington, D. C.: American Geophysical Union. https://doi.org/10.1029/2008GM000843

Sauter, D., Cannat, M., Rouméjon, S., Andreani, M., Birot, D., Bronner, A., Brunelli, D., Carlut, J., Delacour, A., Guyader, V., MacLeod, C. J., Manatschal, G., Mendel, V. Ménez, B., Pasini, V., Ruellan E., & Searle, R. (2013). Continuous exhumation of mantle-derived rocks at the southwest Indian ridge for 11 Million Years. *Nature Geosciences*, *6*, 314–320. https://doi.org/10.1038/ngeo1771

Sauter, D., Mendel, V., Rommevaux-Jestin, C., Parson, L. M., Fujimoto, H., Mével, C., Cannat, M., & Tamaki, K. (2004). Focused magmatism versus amagmatic spreading along the ultra-slow spreading southwest Indian ridge: Evidence from TOBI side scan sonar imagery. *Geochemistry, Geophysics, Geosystems*, *5*(10), Q10K09. https://doi.org/10.1029/2004GC000738

Schlindwein, V., & Schmid, F. (2016). Mid-ocean-ridge seismicity reveals extreme types of ocean lithosphere. *Nature*, *535*, 276-279. https://doi.org/10.1038/nature18277

Schmid, F., & Schlindwein, V. (2016). Microearthquake activity, lithospheric structure, and deformation modes at an amagmatic ultraslow spreading southwest Indian ridge segment. *Geochemistry, Geophyics., Geosystems*, *17*(7), 2905–2921. https://doi.org/10.1002/2016GC006271

Schmid, F., Schlindwein, V., Koulakov, I., Plötz, A., & Scholz, J.-R. (2017). Magma plumbing system and seismicity of an active mid-ocean ridge volcano. *Scientific Reports*, *7*, 42949. https://doi.org/10.1038/srep42949

Schuiling, R. D. (1964). Serpentinization as a possible cause of high heat-flow values in and near the oceanic ridges. *Nature*, *201*, 807–808. https://doi.org/10.1038/201807b0

Schweitzer, J. (2001). Hyposat - An enhanced routine to locate seismic events. *Pure and Applied Geophysics*, *158*(1-2), 277-289. https://doi.org/10.1007/PL00001160

Shi, Y., & Bolt, B. A. (1982). The standard error of the magnitude-frequency *b* value. *Bulletin of the Seismological Society of America*, *72*(5), 1677–1687.

Sibson, R. H. (1998). Brittle failure mode plots for compressional and extensional tectonic regimes. *Journal of Structural Geology*, *20*(5), 655-660. https://doi.org/10.1016/S0191-8141(98)00116-3

Solomon, S.C. (1989). Just how do ocean ridges vary?: Characteristic and population statistics of ocean ridges. In: *Drilling the Oceanic Crust and Upper Mantle: JOI/USSAC Workshop Report* (WHOI-89-39, pp. 73-74). Woods Hole, Massachusetts: Woods Hole Oceanographic Institution.

Tarantola, A. & Valette, B. (1982). Inverse problems = quest for information, *Journal of Geophysics*, *50*(1), 159-170.

Tucholke, B. E., Behn, M. D., Buck, W. R., & Lin, J. (2008). Role of melt supply in oceanic detachment faulting and formation of megamullions. *Geology*, *36*(6), 455-458. https://doi.org/10.1130/G24639A.1

Wiemer, S., & Wyss, M. (2000). Minimum magnitude of completeness in earthquake catalogs: examples from Alaska, the western United States, and Japan. *Bulletin of the Seismological Society of America*, *90*(4), 859–869. https://doi.org/10.1785/0119990114

Woessner, J., & Wiemer, S. (2005). Assessing the quality of earthquake catalogues: Estimating the magnitude of completeness and its uncertainty. *Bulletin of the Seismological Society of America*, *95*(2), 684–698. https://doi.org/10.1785/0120040007

Wyss, M., Hasegawa, A., Wiemer, S., & Umino, N. (1999). Quantitative mapping of precursory seismic quiescence before the 1989, M 7.1 off-Sanriku earthquake, Japan. *Annals of Geophysics*, *42*(5), 851-869.